

1 **One-Year Continuous Observations of Near-Surface Atmospheric**
2 **Water Vapor Stable Isotopes at Matara, Sri Lanka Reveal a Strong**
3 **Link to Moisture Sources and Convective Intensity**

4 Yuqing Wu ^{1,2}, Jing Gao ^{1,3,*}, Aibin Zhao ¹, Xiaowei Niu ¹, Yigang Liu ¹,
5 ², Disna Ratnasekera ^{4,5}, Tilak Priyadarshana Gamage ⁶, Amarasinghe
6 Hewage Ruwan Samantha ⁶

7 *1 State Key Laboratory of Tibetan Plateau Earth System, Resources and Environment,*
8 *Institute of Tibetan Plateau Research, Chinese Academy of Sciences, Beijing 100101,*
9 *China*

10 *2 University of the Chinese Academy of Sciences, Beijing, 100049, China*

11 *3 Lanzhou University, Lanzhou 733000, China*

12 *4 China-Sri Lanka Joint Center for Education & Research, Guangzhou 510301, China*

13 *5 Department of Agricultural Biology, Faculty of Agriculture, University of Ruhuna,*
14 *Matara 81000, Sri Lanka*

15 *6 Faculty of Fisheries and Marine Sciences & Technology, University of Ruhuna,*
16 *Matara 81000, Sri Lanka*

17 ** Corresponding author: Jing Gao (gaojing@itpcas.ac.cn)*

18

19 **Abstract:**

20 Atmospheric water vapor stable isotopes are crucial for understanding
21 hydrological cycle processes under climate change. This study presents the results from
22 a year-long in-situ monitoring of atmospheric water vapor stable isotopes ($\delta^{18}\text{O}$, δD) at
23 Matara, Sri Lanka, from March 2020 to February 2021 to assess how oceanic sources
24 and moisture transport influence coastal atmospheric moisture isotopic composition.
25 We identified clear seasonal patterns in the isotopic composition, with $\delta^{18}\text{O}$, δD , and d-
26 excess showing substantial variation between the southwest and northeast monsoon
27 periods. The primary moisture sources were the Arabian Sea and the Indian Ocean

28 during the southwest monsoon (May to September), characterized by small amplitude
29 fluctuations of $\delta^{18}\text{O}$ (-20.4‰ to -9.1‰). During the northeast monsoon, the northern
30 Bay of Bengal, the Indian subcontinent, and Southeast Asia were primary moisture
31 sources, resulting in large amplitude fluctuations in $\delta^{18}\text{O}$ (-23.9‰ to -7.5‰) and higher
32 d-excess values (up to 25 ‰). The study also identified significant influences of sea
33 surface temperature and sea surface relative humidity on the isotopic composition of
34 water vapor. Additionally, we could use outgoing longwave radiation (OLR) to gauge
35 the intensity of convective activity. Observational periods with low OLR, indicative of
36 stronger and deeper convection, were associated with air masses that were more
37 depleted in $\delta^{18}\text{O}$ than periods with high OLR. These findings facilitate a better
38 understanding of how the monsoon and local meteorological conditions affect water
39 vapor isotope compositions in tropical region. Furthermore, the new dataset will enable
40 to improve water vapor isotopic modeling and projections of atmospheric processes in
41 coastal regions.

42 **Keywords:** Indian Summer Monsoon, Water Vapor Isotopes, Sea Surface Condition,
43 Convective Activity, Sri Lanka

44

45 **Short Summary**

46 Monitoring of atmospheric water vapor isotopes for one year at Matara, Sri Lanka,
47 revealed clear seasonal variations in $\delta^{18}\text{O}$, δD , and d-excess. The results showed lower
48 amplitudes of $\delta^{18}\text{O}$ during the southwest monsoon and higher amplitudes of $\delta^{18}\text{O}$ and
49 higher d-excess during the northeast monsoon. Sea surface evaporation and regional
50 convective activity significantly influenced the isotopic compositions. Overall, our
51 results facilitate an improved understanding of the impacts of the monsoon and local
52 meteorological conditions on tropical water vapor isotope signals.

53

54 **1 Introduction**

55 The Indian Summer Monsoon (ISM), occurring from June to September, is a
56 pivotal component of the Asian climate system, serving as the primary moisture

57 transport system from the Indian Ocean to the Indian subcontinent and the Tibetan
58 Plateau (TP). Monsoonal precipitation plays a crucial role in agriculture and water
59 resource availability, affecting the welfare of over 1.9 billion people in surrounding
60 countries (Webster et al., 1998; Goswami et al., 2006). The Tibetan climate and
61 hydrology are profoundly influenced by the ISM, as it contributes significantly to the
62 regional water cycle by delivering substantial rainfall during the summer months. This
63 rainfall is essential for maintaining the glaciers and permafrost in the TP, a key water
64 catchment area for many of Asia's largest rivers (Bookhagen and Burbank, 2010). The
65 ISM's intensity and variability can lead to significant fluctuations in water availability,
66 affecting both agriculture and hydropower generation in the region (Singh and
67 Bengtsson, 2004; Gao et al., 2014). Furthermore, the interaction between the ISM and
68 the TP's topography creates unique climatic conditions that influence weather patterns
69 and extreme events in the region (Liu and Chen, 2000).

70 The seasonal precipitation and its origins over the TP are inextricably linked to
71 the dynamics of the ISM (Dai et al., 2021). Previous studies have provided evidence
72 that precipitation over the TP offer insights into the climatic fluctuations and distinct
73 moisture attributes associated with the ISM (Gao et al., 2013; Guo et al., 2017). The
74 summer monsoon brings significant moisture from the Indian Ocean, leading to
75 substantial rainfall over the TP primarily during the monsoon months of June-
76 September (Yao et al., 2012). This seasonal influx of moisture is critical for maintaining
77 the regional hydrological balance and supporting ecosystems. Furthermore, the ISM's
78 intensity and variability significantly influence the interannual and decadal
79 precipitation patterns over the TP, affecting the overall water availability and climatic
80 stability of the region (Kaushal et al., 2018).

81 Amidst the backdrop of global climate change, observing stable isotopes in
82 atmospheric water vapor is vital for monitoring and understanding climate shifts in low-
83 latitude areas (Rahul et al., 2016b). Such research is instrumental for providing a deeper
84 understanding of near-surface water vapor dynamics, pinpointing vapor sources and
85 transport routes, and differentiating between various contributions of atmospheric water

vapor to the water cycle. The stable isotopic composition of precipitation (Rahul et al., 2016a; Cai et al., 2017) and water vapor (Risi et al., 2008; Steen-Larsen et al., 2013b; Rahul et al., 2016b; Lekshmy et al., 2022) serves as a valuable tool for identifying the origins and understanding transmission processes of atmospheric water vapor. Fractionation occurs during various phase transitions, such as sea surface evaporation, condensation in clouds, re-evaporation of raindrops beneath clouds, and diffusive exchanges between water vapor and raindrops in different environments (Stewart, 1975; Benetti et al., 2018; Graf et al., 2019). The occurrence of fractionation unveils investigable spatiotemporal distribution patterns in the water isotopic composition, encompassing water vapor and precipitation. In this context, deuterium excess (d -excess = $\delta D - 8 \times \delta^{18}O$) is a useful parameter for studying kinetic fractionation effects (Dansgaard, 1964). Recent studies have significantly enhanced our understanding of isotopic signals in convective regions, elucidating the complex interactions between moisture processes and isotopic composition in tropical deep convection (Risi et al., 2008; Blossey et al., 2010). Around Barbados, during the winter trade winds, vertical transport and large-scale circulation have been identified as primary drivers of isotopic variability at the cloud base, acting over timescales from hours to days (Bailey et al., 2023; Villiger and Aemisegger, 2024). Investigations into water vapor isotopes in the West African troposphere reveal that both convection and mixing highlight the important role played by large-scale atmospheric circulation processes in the variations of water vapor isotopes (Diekmann et al., 2021; de Vries et al., 2022). The precise mechanisms by which convective activity depletes water vapor and precipitation of heavy isotopes are still under debate. Some researchers have emphasized the significance of condensation levels (Cai and Tian, 2016; Permana et al., 2016; Thompson et al., 2017), while others suggested raindrop re-evaporation and raindrop-vapor isotope exchanges during strong convection as crucial factors (Galewsky et al., 2016). Additionally, unsaturated or mesoscale descending airflows that transport vapor depleted in heavy isotopes to the lower atmosphere also contribute to lower isotope values (Risi et al., 2008; Kurita, 2013). The influence of these processes varies with the

115 intensity of convective activity.

116 Research on water vapor stable isotopes in the marine boundary layer aims to
117 elucidate the processes associated with evaporation in different conditions of vertical
118 stability, wind, sea surface temperature (SST), and relative humidity with respect to the
119 SST (RH_{SST}). The d-excess of evaporated water vapor is mainly impacted by kinetic
120 fractionation and sensitive to SST, RH_{SST} , the wind speed and the turbulence regime in
121 the boundary layer (Merlivat and Jouzel, 1979; Benetti et al., 2015, 2018).
122 Investigations into the water vapor stable isotopic composition within the marine
123 boundary layer have been principally focused on regions such as the North Atlantic
124 (e.g., Greenland, Iceland, Bermuda) (Steen-Larsen et al., 2013a; Bonne et al., 2014;
125 Benetti et al., 2018; Bonne et al., 2019), Bay of Bengal (BoB) (Lekshmy et al., 2022),
126 and Arctic Oceans (Kurita, 2011). Several studies could confirm the existence of a
127 negative relationship between d-excess and RH_{SST} (Uemura et al., 2008; Steen-Larsen
128 et al., 2015), with wind speed and SST exerting a limited influence on this correlation
129 (Benetti et al., 2015). Observations from the North Atlantic support this theory (Benetti
130 et al., 2014). Other studies, argue that the SST does have an influence via the weak
131 dependence of the d-excess on temperature during equilibrium fractionation based on
132 theoretical arguments (Aemisegger and Sjolte, 2018) as well as observations in the
133 marine boundary layer covering a large latitudinal gradient over the Atlantic and
134 Southern Ocean (Thurnherr et al. 2020). In addition, studies found significant variations
135 in d-excess values in vapor that originated at different moisture sources (Pfahl and
136 Wernli, 2008; Kurita, 2011; Steen-Larsen et al., 2013b; Delattre et al., 2015).
137 Subsequently, Benetti et al. (2015) introduced a multi-layer mixing model, which is
138 expected to improve the accuracy of d-excess and water vapor isotope simulations. Due
139 to the impact of kinetic fractionation on sea surface water evaporation, some studies
140 have focused on simulating observed d-excess under the closure assumption (Merlivat
141 and Jouzel, 1979). Others have used isotope atmospheric circulation models to assess
142 mixing and transport processes within the marine boundary layer at different resolution
143 (Steen-Larsen et al. 2017; Risi et al. 2020; Thurnherr et al. 2021). In addition, previous

144 studies have used single column analytical mixing models (Risi et al. 2019), as well
145 trajectory-based box models (Thurnherr and Aemisegger, 2022). Owing to the minor
146 influence of transport-induced fractionation, d-excess in the marine boundary layer is
147 typically employed to deduce moisture sources (Benetti et al., 2018).

148 Located in the northern Indian Ocean, Sri Lanka is impacted by both the southwest
149 and northeast monsoons (Fig. 1a, b) and has been identified as an important origin
150 region for monsoonal water vapor over the TP. However, only few studies have focused
151 on the Indian Ocean, and even fewer on the area around Sri Lanka. This knowledge gap
152 underscores the need to explore isotopic signals in this region and place them into their
153 appropriate context, e.g., with findings by Risi et al. (2008). For instance, more recent
154 studies on water stable isotopes in the South Indian Ocean and South Asian region have
155 uncovered connections between local processes and large-scale atmospheric circulation,
156 shedding light on sea-surface dynamics (Midhun et al., 2013; Rahul et al., 2016b;
157 Bonne et al., 2019). Unlike, in precipitation and surface water, in atmospheric water
158 vapor stable isotopes can be monitored continuously regardless of season, weather, or
159 location (Angert et al., 2008). This potentially full temporal and spatial coverage allows
160 for a more comprehensive and continuous monitoring of atmospheric water vapor
161 dynamics and transport, which should in turn facilitate a deeper understanding of
162 isotope transformation processes within the water cycle. Therefore, investigating the
163 dynamics of near-surface atmospheric water vapor stable isotopes at coastal stations is
164 not only pivotal for identifying monsoonal water vapor source regions but will facilitate
165 a better understanding of precipitation processes over the Indian Ocean. Oceanic
166 evaporation represents the first of many phase transitions that occur during the global
167 water cycle. The primary objective of researching water vapor stable isotopes is to
168 comprehend the processes and controlling factors of water isotopic variations.

169 In this study, we present the results from continuous observations of near-surface
170 atmospheric water vapor stable isotopes in Matara, Sri Lanka, collected from March 1,
171 2020, to February 28, 2021. We analyze the observational data to gain a better
172 understanding of the variations in moisture sources and main transmission processes in

173 tropical coastal regions. Furthermore, we explore how sea surface processes, convective
174 activity, and local meteorological factors affect near-surface atmospheric water vapor
175 stable isotopes at a coastal station, across daily, monthly, and seasonal (monsoonal) time
176 scales. Section 2 gives an overview of the study site and presents the meteorological
177 and water vapor observations, calibration protocols, and analysis methods. In Section
178 3, we illustrate the variability of isotopic and meteorological parameters, analyze
179 moisture sources, assess the impact of sea surface processes on water vapor isotopes,
180 and explore the relationship between water vapor isotopes, convective activity, and
181 local meteorological observations.

182

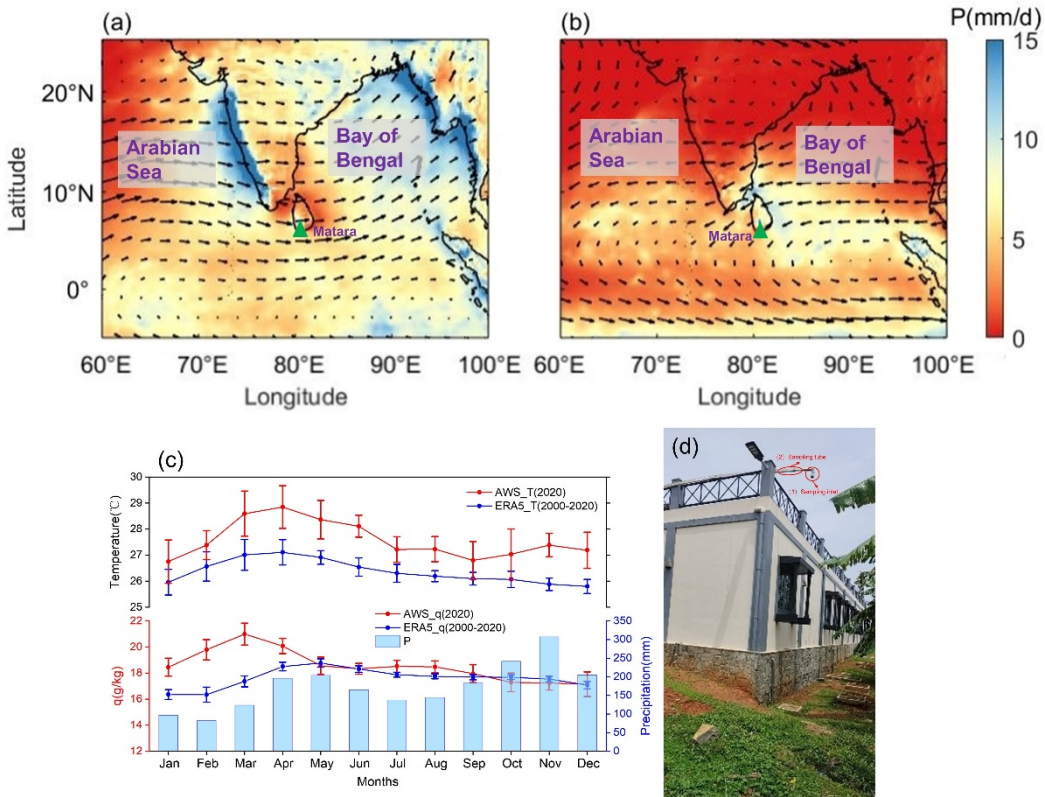
183 **2 Study Site, Data, and Methods**

184 **2.1 Study Site and Meteorological Data**

185 Sri Lanka (located between approximately 6°N to 10°N and 79° to 82°E) is the
186 southernmost country on the Indian subcontinent and a key region for identifying the
187 moisture source of the south Asian summer monsoon (Ravisankar et al., 2015).
188 Featuring a tropical climate, Sri Lanka experiences four distinct monsoon seasons
189 annually: the northeast monsoon from December to February, the first inter-monsoon
190 from March to April, the southwest monsoon from May to September, and the second
191 inter-monsoon from October to November (Malmgren et al., 2003; Jayasena et al.,
192 2008). For the analyses, we combined the first and second inter-monsoon periods into
193 a single “non-monsoon period”. Most of the precipitation in Sri Lanka comes from the
194 southwest and northeast monsoon systems, accounting for over 78% of the total annual
195 precipitation (Fig. 1c). Precipitation formation in Sri Lanka primarily relies on
196 organized convection associated with the Intertropical Convergence Zone (ITCZ) and
197 low-pressure systems (Gadgil, 2003), while the associated moisture primarily originates
198 in the Indian Ocean and BoB (Bandara et al., 2022). The southwest monsoon transports
199 moisture from the Indian Ocean to southwestern Sri Lanka (Fig. 1a) where it leads to
200 increased rainfall (Bavadekar and Mooley, 1981). In contrast, the northeast monsoon
201 carries water vapor from the BoB to northern and northeastern of Sri Lanka (Fig. 1b)

202 (Dhar and Rakhecha, 1983; Wang, 2006).

203 An automated weather station (AWS) was installed at the University of Ruhuna,
204 Matara (located at 5.94°N, 80.57°E) on the southern coast of Sri Lanka (Fig. 1d). It
205 collected real-time meteorological observations, including air temperature,
206 precipitation, relative humidity, air pressure, wind speed, and wind direction, from
207 March 1, 2020, to February 28, 2021.



208

209 **Figure 1: Mean wind vectors (arrows) at 850 hPa during the (a) 2020 southwest monsoon and**
210 **(b) 2020/2021 northeast monsoon seasons, along with mean precipitation (P, base colors) from**
211 **ERA5 averaged for the same period. (c) Monthly mean temperature and specific humidity (q)**
212 **obtained from the automated weather station at Matara (January and February are from 2021**
213 **while March – December from 2020), with monthly average temperature, specific humidity,**
214 **and precipitation from ERA5 (averaged for the years 2000-2020) plotted for comparison. (d)**
215 **Photograph of the roof-mounted weather station at the University of Ruhuna, Sri Lanka.**

216 In this study, we used hourly data of 2m air temperature, 2m dew temperature, air
217 pressure, precipitation, SST, atmospheric boundary layer height (BLH), wind speed,
218 wind direction, and outgoing longwave radiation (OLR), obtained from ERA5 for years

219 2000 to 2021, with a spatial resolution of $0.25^\circ \times 0.25^\circ$ and a temporal resolution of one
 220 hour. Meteorological data are compared with water vapor isotopic data measured during
 221 the same period. Based on the European Centre for Medium-Range Weather Forecasts
 222 (ECMWF, <https://cds.climate.copernicus.eu/eu/>) reanalysis dataset (ERA5), the annual
 223 average precipitation and air temperature for the period from 2000 to 2020 is 2085 mm
 224 and 27.6°C , respectively (Fig. 1c) (Hersbach et al., 2020). Studies have shown that
 225 ERA5 data provide good representations of the Matara equatorial climate and can be
 226 used in lieu of missing observational data (Fig. S3) (Bandara et al., 2022). Due to
 227 weather conditions and instrument trouble, specific humidity measured by the isotopic
 228 measurement instrument and computed by the AWS are missing from March, 2020 to
 229 April, 2020. Therefore, we chose to present both variables obtained from ERA5 as they
 230 complement each other, providing a clearer picture of humidity changes at Matara
 231 station.

232 For the atmosphere above open sea regions, RH_{SST} is obtained using (Bonne et al.,
 233 2019):

$$\text{RH}_{\text{SST}} = \text{RH}_{2\text{m air}} \times \frac{q_{\text{sat}}(T_{2\text{m air}})}{q_{\text{sat}}(\text{SST})} \quad (6)$$

234 where RH_{2m air} is the relative humidity 2m above the ocean surface, q_{sat}(T_{2m air}) is
 235 the specific humidity at a saturated condition for a given 2m air temperature, and
 236 q_{sat}(SST) is calculated for seawater with a salinity of 35 practical salinity units (PSU)
 237 (Curry and Webster, 1999).

238 The formulas to calculate air saturation specific humidity q_{sat}(T_{2m air}) and sea
 239 surface saturation specific humidity q_{sat}(SST) with a salinity of 35 PSU are:

$$q_{\text{sat}}(T_{2\text{m air}}) = \frac{0.622 \times E}{P} \quad (7)$$

$$q_{\text{sat}}(\text{SST}) = 0.98 \times q_s \quad (8)$$

240 q_s represents specific humidity with a salinity of 35 PSU and is calculated in the same
 241 way as q_{sat}(T_{2m air}). E is the saturated water vapor pressure, obtained from the

242 improved Goff-Gratch formula (Goff and Gratch, 1946). P is atmospheric pressure. We
243 take the sea surface pressure as the atmospheric pressure to participate in the above
244 calculation (Eq. 7).

245 **2.2 In-situ Observations of Atmospheric Water Vapor Isotopic
246 Composition**

247 Near-surface atmospheric water vapor isotope measurements at Matara were
248 collected using a sampling frequency of 1Hz with the instrument located approximately
249 5m from the AWS. We used a Water Vapor Isotope Analyzer (Los Gatos Research (LGR)
250 Inc.) in conjunction with an LGR Water Vapor Isotope Standard Source (WVISS) model.
251 The LGR instrument employs a mirrored sampling chamber in which the laser traverses
252 the sample volume thousands of times, effectively amplifying the water vapor
253 absorption signal which facilitates the detection of low concentrations of D and ^{18}O
254 (Liu et al., 2015). Compared to traditional methods, this spectroscopic technique offers
255 three advantages: (i) it is compact and portable, enabling real-time field monitoring; (ii)
256 it can simultaneously measure $\delta^{18}\text{O}$ and δD ; and (iii) it has lower measurement costs
257 and requires less operator expertise.

258 The instrumental setup was situated approximately 100 m from the sea shore (5.94°
259 N, 80.57° E, 10 meters), and consisted of four primary components: (1) A sampling
260 inlet, positioned approximately 5 m above the ground (Fig. 1d), equipped with a
261 stainless-steel mesh to prevent interference from insects and facing downward to avoid
262 direct impacts from rain. (2) A 1/4-inch outer diameter stainless steel sampling tube,
263 insulated with heating tape and a 2-cm thick pipe for thermal insulation. (3) The
264 calibration unit to generate a constant flow of water vapor with known isotopic
265 composition and at different humidity levels. (4) A water vapor isotope analyzer,
266 delivering a measurement precision for $\delta^{18}\text{O}$ and δD of 0.25‰ and 0.5‰, respectively
267 (a concentration of 2500 ppmv). This setup has been designed to minimize external
268 influences and maintain the integrity of the sampled water vapor.

269 The spatial proximity between the water vapor analyzer and AWS ensures a high
270 level of synchronicity between the isotope and meteorological measurements. We

271 define wind directions from 60° to 330°N as oceanic, while those from 330° to 60°N as
272 terrestrial winds (Fig. 1a, b).

273 Atmospheric water vapor stable isotopes are expressed using the δ notation (in per
274 mil, ‰), using the following equations:

$$R_{^{18}O} = \frac{^{18}O}{^{16}O} \quad (9)$$

$$R_D = \frac{D}{^1H} \quad (10)$$

$$\delta_{\text{sample}} = \left(\frac{R_{\text{sample}}}{R_{\text{VSMOW}}} - 1 \right) \times 1000\% \quad (11)$$

275 Here, δ_{sample} represents either $\delta^{18}O$ or δD (^{18}O or D isotope ratio) relative to Vienna
276 Standard Mean Ocean Water (VSMOW). R_{sample} and R_{VSMOW} are the ^{18}O or D and
277 VSMOW isotope ratios, respectively.

278 2.3 Calibration Protocol

279 In this study, we adhere to the calibration protocol proposed by Steen-Larsen et al.
280 (2013b). Briefly, the instrument calibration and data processing consist of three major
281 steps: (1) humidity-isotope response calibration, (2) VSMOW - Standard Light
282 Antarctic Precipitation (VSMOW-SLAP) calibration, and (3) drift correction (see Text
283 S1 in the Supporting Information).

284 The water vapor concentration can influence the measured water vapor isotopic
285 composition, known as concentration- or humidity-isotope dependency
286 characterization. By adding a constant stream of water vapor with known isotopic
287 composition at different humidity levels, we can establish the humidity-isotope
288 response function (Sturm and Knohl, 2010; Aemisegger et al., 2012). As this function
289 can vary over time, its calibration was repeated monthly, using two standard samples of
290 known isotopic compositions measured at humidity levels ranging from 16,000 to
291 38,000 ppmv at intervals of 1000 ppmv. Each level was measured for at least 25 minutes
292 using the LGR WVISS. Our results are referenced to a humidity level of 20,000 ppmv.
293 We compared our measurements to the international VSMOW-SLAP scale, assuming a
294 linear drift between calibration points.

295 To compensate for instrumental drift, we measured the water vapor from a drift-
 296 standard bottle for 25 minutes after each 12 hours performed an ambient air
 297 measurement. Furthermore, we tested for instrument drift as part of the routine
 298 instrument maintenance, assuming a linear drift between each drift-standard
 299 measurement. Laboratory analyses of liquid isotopes have confirmed the stability of its
 300 isotopic composition over time.

301 **2.4 Rayleigh Distillation Model and MBL-Mixing Model**

302 The Rayleigh distillation model is employed to quantify isotopic variations during
 303 phase changes (Dansgaard, 1964), by which the residual air mass becomes drier with a
 304 depletion in heavy isotopes following moist adiabatic vertical ascent (Gat, 1996):

$$R_r = R_0 f^{\alpha_v^l(T)} - 1 \quad (12)$$

305 Here, R_r and R_0 represent the isotopic ratio of residual vapor and initial vapor,
 306 respectively. $\alpha_v^l(T)$ denotes the equilibrium fractionation factor, and f is the fraction
 307 of residual water vapor.

308 By integrating the definition of isotope ratios as given in Equation (11), the
 309 Rayleigh distillation model can be expressed in terms of isotopic content as follows:

$$\delta_r = (\delta_0 + 1) f^{\alpha_v^l(T)} - 1 \quad (13)$$

310 where δ_r and δ_0 are the isotope ratios relative to VSMOW in residual and initial vapor,
 311 respectively.

312 We employ the mixing model to examine the isotopic characteristics after the
 313 mixing of two air masses (Galewsky and Hurley, 2010):

$$R_{\text{mix}} = \frac{f[\text{HDO}]_1 + (1 - f) \times [\text{HDO}]_2}{f[\text{H}_2\text{O}]_1 + (1 - f) \times [\text{H}_2\text{O}]_2} \quad (14)$$

$$R_{\text{mix}} = \frac{f[\text{H}_2^{18}\text{O}]_1 + (1 - f) \times [\text{H}_2^{18}\text{O}]_2}{f[\text{H}_2\text{O}]_1 + (1 - f) \times [\text{H}_2\text{O}]_2} \quad (15)$$

314 where R_{mix} represents the isotopic ratio of the mixed air mass, while $[\text{HDO}]$, $[\text{H}_2\text{O}]$, and
 315 $[\text{H}_2^{18}\text{O}]$ denote isotopic water vapor volume mixing ratios, and f is the mixing fraction.
 316 The isotopic ratio and isotopic δ in the Eq. 14 and Eq. 15 have been calibrated by
 317 VSMOW.

318 We use water vapor isotopes to characterize the mixing processes in the marine
319 boundary layer (MBL) (Benetti et al., 2018), using the following equation (Craig and
320 Gordon, 1965):

$$1 + \delta_e = \frac{1}{\alpha_k} \times \frac{\alpha_v^l \times (1 + \delta_{OC}) - RH_{SST} \times (1 + \delta_{MBL})}{1 - RH_{SST}} \quad (16)$$

321 where α_v^l represents the equilibrium fractionation factor between vapor and liquid, and
322 α_k is the kinetic fractionation factor. δ_{OC} denotes the isotopic composition of the ocean
323 surface. We utilize α_v^l from Majoube (1971a, b) and α_k for the smooth regime ($\alpha_k^{18O} =$
324 1.006 and $\alpha_k D = 1.0053$) (Merlivat and Jouzel, 1979).

325 **2.5 Qualitative Trajectory-based Moisture Source Analysis**

326 To delineate water vapor transport paths and pinpoint moisture sources, we
327 employed the Hybrid Single-Particle Lagrangian Integrated Trajectory (HYSPLIT)
328 model from the US National Oceanic and Atmospheric Administration (NOAA) to
329 compute backward trajectories of air masses arriving at Matara station during the
330 southwest and northeast monsoons. The Global Data Assimilation System (GDAS) with
331 $1^\circ \times 1^\circ$ and 3-hour spatial and temporal resolutions provided the background
332 meteorological data from May 2020 to September 2020 and December 2020 to
333 February 2021 (<ftp://arlftp.arlhq.noaa.gov/archives/gdas1/>). The HYSPLIT model uses
334 GDAS reanalysis data, which contains 37 (vertical) pressure levels and a $1^\circ \times 1^\circ$
335 horizontal resolution. Atmospheric water vapor primarily resides at altitudes below 2
336 km (Wallace and Hobbs, 2006). In this study, particles were released four times daily
337 (at 00:00, 06:00, 12:00, and 18:00 UTC) at 20 different locations within a rectangular
338 area extending 0.2° in each direction (north, south, east, and west) from Matara station
339 and at four heights above the ground (50 m, 500 m, 1200 m, and 2000 m). Each
340 trajectory was back-traced for 168 h, recording data at 1-h intervals. The HYSPLIT
341 model outputs latitude, longitude, elevation, pressure, temperature, precipitation,
342 relative humidity, and specific humidity. Backward trajectory clustering analysis was
343 conducted, using the corresponding meteorological data. We averaged the trajectories
344 of four times per day to obtain a daily mean trajectory, combined with water vapor

345 stable isotope values on precipitation days. These daily mean trajectories were clustered
346 by moisture source using K-means clustering. By analyzing the variations in latitude,
347 elevation, and specific humidity along the trajectories, the influence of different
348 moisture sources on local vapor content and isotopic composition was evaluated.

349 These analyses yielded concentration-weighted trajectory (CWT) fields
350 (resolution of $0.5^\circ \times 0.5^\circ$) (Hsu et al., 2003) using the in-situ daily average $\delta^{18}\text{O}$ and d-
351 excess, which in turn facilitated the identification of potential moisture sources and an
352 assessment of the potential influence of recirculation on d-excess in water vapor
353 (Salamalikis et al., 2015; Bedaso and Wu, 2020; Xu et al., 2022). CWT (C_{ij}) was
354 calculated as:

$$C_{ij} = \frac{\sum_{k=1}^K C_k \tau_{ijk}}{\sum_{k=1}^K \tau_{ijk}} \quad (17)$$

355 where (i, j) denote grid coordinates, k the trajectory index, K the total number of
356 trajectories analyzed, C_k the concentration (here $\delta^{18}\text{O}$ and d-excess) at the end of the
357 trajectory k , and τ_{ijk} the residence time of trajectory k in grid cell (i, j) . We substituted
358 the residence time by the number of trajectory endpoints in each grid cell (i, j) .

359

360 **3 Results**

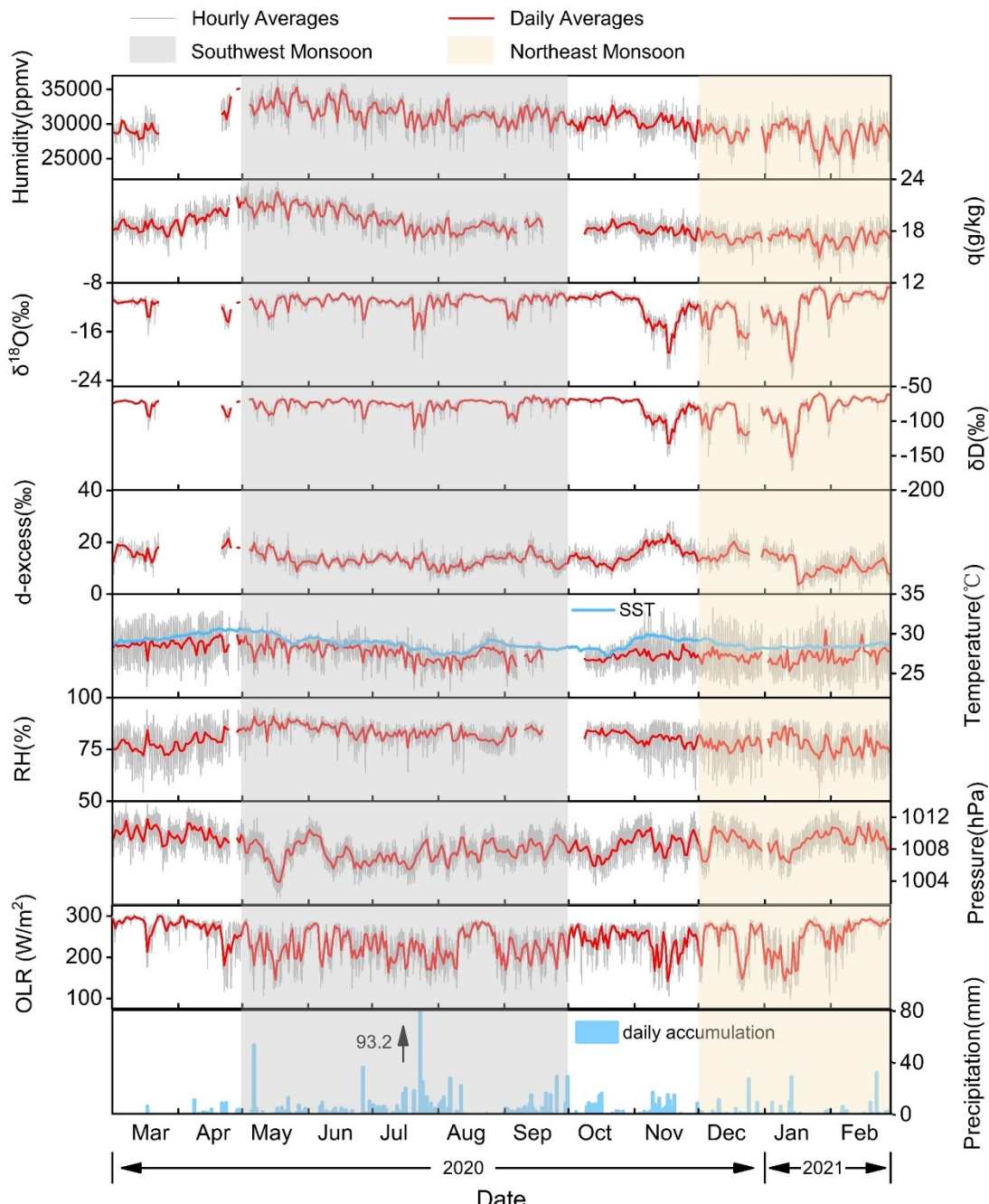
361 **3.1 Seasonal Variability of Water Vapor Stable Isotope**

362 During a year-long observational period (1 March 2020 to 28 February 2021), the
363 seasonal and synoptic variations observed in water vapor isotopes ($\delta^{18}\text{O}$, δD , and d-
364 excess) and key meteorological parameters (temperature, relative humidity,
365 atmospheric pressure, specific humidity, and SST) are explored (Fig. 2), aiming to
366 provide insights into the interactions between atmospheric and oceanic conditions at
367 Matara. The tropical setting at Matara leads to relatively modest temperature
368 fluctuations, with the 12-month average at 27.6°C , dipping to 22.3°C and reaching 33.5°C
369 at extremes. The amplitude of temperature remains around 10°C between monsoon and
370 non-monsoon periods. Specific humidity ranging from 16 g/kg to 21 g/kg and shows
371 marked oscillations during the southwest and northeast monsoons, with amplitudes of

372 approximately 1.3 g/kg and 2.3 g/kg, respectively. Relative humidity also shows clear
373 seasonal pattern, peaking at 95% in May (southwest monsoon) and falling to 49.2% in
374 January (northeast monsoon). Monthly trends (Fig. S4 and Table 1) reveals a steady
375 decrease in both air temperature and specific humidity from May to September,
376 culminating in their lowest values (26.9°C and 18.5 g/kg, respectively). During the
377 southwest monsoon, temperatures and specific humidity in May (monthly averages of
378 $28.4 \pm 1.4^\circ\text{C}$ and $21.0 \pm 1.1 \text{ g/kg}$) reflect the influx of warm, moist air from the Indian
379 Ocean. In contrast, February stands out as the coldest and driest period ($27.4 \pm 2.6^\circ\text{C}$
380 and $17.1 \pm 1.3 \text{ g/kg}$) corresponding to the northeast monsoon (Fig. S4). Among them,
381 daily average SSTs consistently exceed the daily average 2m air temperatures recorded
382 by the AWS, indicating the ocean's significant role in modulating near-surface
383 atmospheric conditions (Fig. 2).

384 Yearly averages for water vapor isotopic values are $-11.6\text{\textperthousand}$ for $\delta^{18}\text{O}$, $-79.5\text{\textperthousand}$ for
385 δD , and $13.3\text{\textperthousand}$ for d-excess, respectively. Isotopic composition ranges from $-23.9\text{\textperthousand}$ to
386 $-7.5\text{\textperthousand}$ for $\delta^{18}\text{O}$, $-173.2\text{\textperthousand}$ to $-53.4\text{\textperthousand}$ for δD , and $-1.2\text{\textperthousand}$ to $28.1\text{\textperthousand}$ for d-excess (Table
387 1). Monthly averages of water vapor isotopes ($\delta^{18}\text{O}$ and d-excess) exhibit stability from
388 March to October, followed by sudden decreases. $\delta^{18}\text{O}$ and δD show distinct seasonal
389 variations, with higher values during the southwest monsoon and lower values during
390 the northeast monsoon (Table 1). Therefore, the subsequent analysis will concentrate
391 on the variations in $\delta^{18}\text{O}$. During the southwest monsoon, the northeast monsoon, and
392 the non-monsoon periods, the average values of $\delta^{18}\text{O}$ are $-11.1\text{\textperthousand}$, $-12.2\text{\textperthousand}$, and $-11.9\text{\textperthousand}$,
393 respectively. Extreme values of $\delta^{18}\text{O}$ are observed during the northeast monsoon, with
394 a maximum of $-7.5\text{\textperthousand}$ and a minimum of $-23.9\text{\textperthousand}$. Conversely, d-excess exhibits a
395 reverse pattern to $\delta^{18}\text{O}$ on both seasonal and monthly scales, characterized by lower
396 values during the southwest monsoon and higher values during the non-monsoon period.
397 Furthermore, during the northeast monsoon, the southwest monsoon, and the non-
398 monsoon periods, the average values of d-excess are $12.4\text{\textperthousand}$, $13\text{\textperthousand}$, and $14.7\text{\textperthousand}$,
399 respectively. The d-excess maximum occurs in November at $28.1\text{\textperthousand}$ (monthly average
400 of $15.2 \pm 4.3\text{\textperthousand}$), while the minimum of $-1.2\text{\textperthousand}$ was recorded in January (monthly

401 average of $11.3 \pm 4.5\text{‰}$). The high values of d-excess are related to moisture recycling.
 402 Low specific humidity corresponds to depleted $\delta^{18}\text{O}$ and elevated d-excess, indicating
 403 a strong depletion during the long-distance transport from the source regions to the
 404 observation station. Coastal stations such as Bangalore, Ponmudi, and Wayanad also
 405 show similar water vapor isotopic depletion in autumn and winter, reflecting the
 406 observations made at Matara (Table 2).



407
 408 **Figure 2: Near-surface observations at Matara station of water vapor isotopes ($\delta^{18}\text{O}$, δD , and**

409 **d-excess) and meteorological parameters (humidity, specific humidity (q), temperature,**
410 **relative humidity (RH), pressure, outgoing longwave radiation (OLR, obtained from NCEP),**
411 **and precipitation) from March 1, 2020, to February 28, 2021. Local sea surface temperature**
412 **at Matara (SST, obtained from ERA5) is plotted in blue.**

413 For $\delta^{18}\text{O}$, δD , and d-excess, synoptic variations were recorded (Fig. 2). Abrupt
414 changes occurred in late July 2020 and from November 2020 to January 2021,
415 associated with synoptic events. Cumulative precipitation in July 2020 reached 451.8
416 mm, with a notable rainfall event in late July recording daily rainfall of 93.2 mm.
417 Isotopic $\delta^{18}\text{O}$ values show a sharp depletion from $-10.4\text{\textperthousand}$ to $-20.4\text{\textperthousand}$ within 20 h of
418 isolated rainfall events, lasting for 6 days. Over the 75-day period spanning from late
419 southwest monsoon to mid-northeast monsoon, significant fluctuations can be seen in
420 isotopic $\delta^{18}\text{O}$ between $-22\text{\textperthousand}$ and $-11\text{\textperthousand}$. During the southwest monsoon from July 12
421 to August 7, $\delta^{18}\text{O}$ values varied from $-20.4\text{\textperthousand}$ to $-9.2\text{\textperthousand}$, and δD values ranged from -
422 $143.5\text{\textperthousand}$ to $-68.6\text{\textperthousand}$. This finding is consistent with water vapor isotopic $\delta^{18}\text{O}$ ($-14.1\text{\textperthousand}$
423 to $-9.8\text{\textperthousand}$) and δD ($-97.2\text{\textperthousand}$ to $69.1\text{\textperthousand}$) values measured from July 12 to August 7, 2012,
424 near the Bay of Bengal, although the local minimum at Matara station is below the
425 minimum in the Bay of Bengal (Midhun et al., 2013).

426 **Table 1: Summary of hourly-averaged data collected at Matara station from March 1, 2020,**
 427 **to February 28, 2021. Averages are shown in bold. N indicates the number of observations of**
 428 **$\delta^{18}\text{O}$, δD , d-excess, temperature (T), relative humidity (RH), specific humidity (q), and**
 429 **atmospheric boundary layer height (BLH). Yearly maxima and minima for each parameter**
 430 **are highlighted using bold italics.**

| Season | | $\delta^{18}\text{O}$ | δD | d-excess | T | RH | q | BLH |
|----------------------|------|-----------------------|------------------|-------------|-------------|-------------|-------------|---------------|
| | | (‰) | (‰) | (‰) | (°C) | (%) | (g/kg) | (m) |
| Non- monsoon | mean | -11.9 | -80.6 | 14.7 | 28.0 | 79.4 | 18.6 | 630.1 |
| | SD | 2.2 | 16.6 | 3.8 | 2.2 | 7.3 | 1.3 | 179.1 |
| | Max. | -9.0 | -65.3 | 28.1 | 33.2 | 94.2 | 23.0 | 1178.8 |
| | Min. | -22.1 | -151.1 | 5.1 | 23.3 | 54.2 | 15.1 | 84.4 |
| | N | 1851 | 1851 | 1851 | 2617 | 2617 | 2617 | 2928 |
| Southwest monsoon | mean | -11.1 | -75.7 | 13.0 | 27.6 | 83.8 | 19.4 | 741.4 |
| | SD | 1.3 | 9.6 | 2.8 | 1.5 | 4.5 | 1.5 | 149.0 |
| | Max. | -9.1 | -60.8 | 24.1 | 32.7 | 95.0 | 23.7 | 1564.4 |
| | Min. | -20.4 | -143.5 | 4.5 | 22.7 | 63.4 | 15.1 | 259.0 |
| | N | 3314 | 3314 | 3314 | 3192 | 3197 | 3192 | 3672 |
| Northeast monsoon | mean | -12.2 | -85.1 | 12.4 | 27.1 | 77.4 | 17.2 | 516.4 |
| | SD | 3.0 | 22.0 | 4.29 | 2.4 | 7.8 | 1.2 | 139.4 |
| | Max. | -7.5 | -53.4 | 25.0 | 33.5 | 90.0 | 19.9 | 1125.7 |
| | Min. | -23.9 | -173.2 | -1.2 | 22.3 | 49.2 | 13.1 | 182.0 |
| | N | 1885 | 1885 | 1885 | 1993 | 1993 | 1993 | 2160 |
| All | mean | -11.6 | -79.5 | 13.3 | 27.6 | 80.7 | 18.6 | 648.7 |
| | SD | 2.2 | 16.1 | 3.6 | 2.0 | 7.0 | 2.1 | 181.3 |
| | Max. | -7.5 | -53.4 | 28.1 | 33.5 | 95.0 | 23.7 | 1564.4 |
| | Min. | -23.9 | -173.2 | -1.2 | 22.3 | 49.2 | 13.1 | 84.4 |
| | N | 7050 | 7050 | 7050 | 7802 | 7807 | 7807 | 8760 |

431

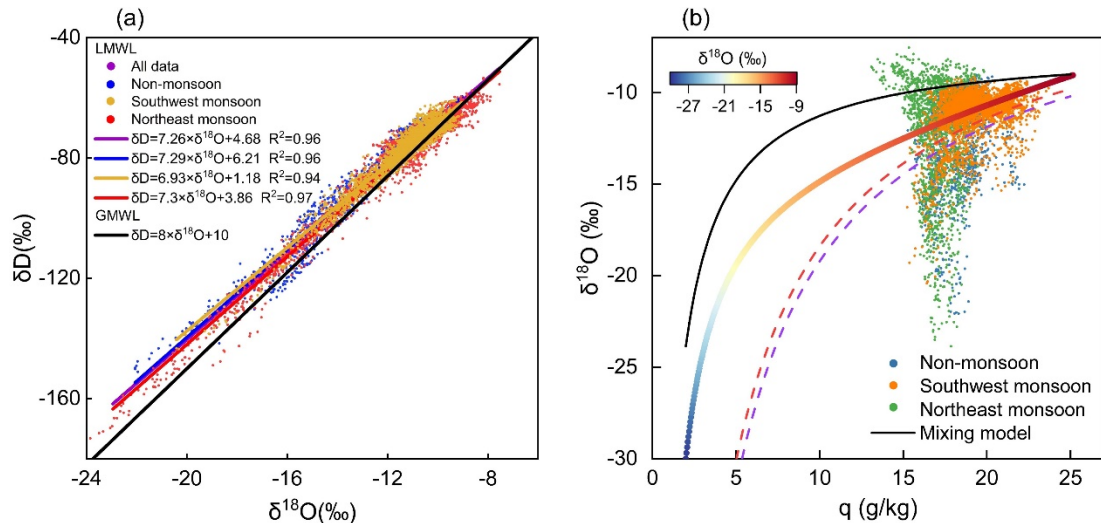
432 The atmospheric water vapor line serves as an indicator of the humidity conditions
433 at the vapor source and the fractionation processes along the transport path. The slope
434 reflects the extent of vapor kinetic fractionation, while the intercept indicates the
435 humidity levels at the vapor source. Comparing the Local Meteoric Water Line (LMWL)
436 for $\delta^{18}\text{O}$ and δD with the Global Meteoric Water Line (GMWL) we obtain a slope of <
437 8 during both monsoon periods (Fig. 3a). Seasonal variations are also visible in $\delta^{18}\text{O}$
438 and δD distribution patterns. Daily averages of water vapor isotopic $\delta^{18}\text{O}$ and δD
439 demonstrate a strong correlation ($r = 0.96$, slope = 7.26) with a lower intercept at 4.68.
440 The LMWL slope and intercept vary significantly between monsoon and non-monsoon
441 seasons, peaking in the northeast monsoon with values of 7.3 and 3.86, and nadir in the
442 southwest monsoon with 6.93 and 1.18, respectively. This suggests increased humidity
443 over sea surface vapor sources from the northeast to southwest monsoon, attributed to
444 heightened evaporation and reduced dynamic fractionation effects. During the northeast
445 monsoon, LMWL slope and intercept are higher compared to other periods, indicating
446 significant moisture recirculation.

447 **Table 2: Summary of observed water vapor isotope concentrations at various stations in India**
448 **and the Bay of Bengal.**

| Country or region | Station or location | Latitud e (N°) | Longitu de (E°) | Date | $\delta^{18}\text{O}$ (‰) | δD (‰) | d-excess (‰) | References |
|-------------------|---------------------|----------------|-----------------|------------------|---------------------------|----------------------|--------------|-----------------------------|
| India | Bangalore | 13.01 | 77.55 | Jun 1, 2012, to | -23.8 | -178.3 | -4.5 to | |
| | | | | Sep 30, 2012 | to -9.0 | to -58.6 | 32.7 | |
| | | | | Oct 1, 2012, to | -22.7 | -177.1 | -9.5 to | (Rahul et al., 2016b) |
| | | | | Feb 28, 2013 | to -10.2 | to -73.7 | 41.4 | |
| | Kolkata | 22.56 | 88.41 | May 3, 2019, to | -16.9 | -128.3 | -7.1 to | |
| | | | | Oct 25, 2019 | to -10.0 | to -72.8 | 25.4 | (Bhattacharya et al., 2021) |
| | Roorkee | 29.87 | 77.88 | Feb 1, 2007, to | -17.0 | | 32.0 to | |
| | | | | May 31, 2007 | to -3.0 | | 70.0 | |
| | | | | Jun 1, 2007, to | -32.0 | none | 40.0 to | |
| | | | | Sep 30, 2007 | to -6.0 | | 87.0 | (Saranya et al., 2018) |
| Bay of Bengal | Ponmudi | 8.76 | 77.12 | Oct 1, 2007, to | -30.0 | | 30.0 to | |
| | | | | Dec 31, 2007 | to -7.0 | | 60.0 | |
| | Wayanad | 11.51 | 76.02 | Apr 1, 2012, to | -24.1 | -170.0 | 6.3 to | |
| | | | | Nov 30, 2012 | to -8.6 | to -51.0 | 26.5 | (Lekshmy et al., 2018) |
| | Ahmedabad | 23.03 | 72.56 | Apr 1, 2007, to | -20.5 | -139.1 | 13.3 to | |
| | | | | Apr 1, 2008 | to -7.9 | to -50.0 | 31.2 | |
| | Chhota Shigri | 32.58 | 77.58 | Apr 1, 2007, to | -19.2 | -128.1 | 6.9 to | |
| | | | | Apr 1, 2008 | to -8.9 | to -59.8 | 40.4 | (Srivastava et al., 2015) |
| | 6m | 32.58 | 77.58 | Apr 1, 2007, to | -19.4 | -101.5 | 28.0 to | |
| | | | | Apr 1, 2008 | to -10.3 | to -29.2 | 62.0 | (Ranjan et al., 2021) |
| Bay of Bengal | 25m | 25m | none | Jul 1, 2012, to | -13.6 | -94.0 to | 5.7 to | |
| | | | | Aug 1, 2012 | to -10.0 | -68.3 | 16.4 | (Midhun et al., 2013) |
| | 25m | 25m | none | Nov 15, 2013, to | -14.1 | -97.2 to | 6.9 to | |
| | | | | Dec 1, 2013 | to -9.8 | -69.1 | 19.4 | |

449 We found a significant negative relationship between d-excess and $\delta^{18}\text{O}$, with a
450 rate of change for d-excess with $\delta^{18}\text{O}$ is $-0.68 \text{‰}/\text{‰}$ ($r = -0.55$) (Fig. S5a). This below
451 the $-0.05 \text{‰}/\text{‰}$ recorded at Bangalore station (Rahul et al., 2016b). Seasonally, the
452 correlation between both variables have weaken during the southwest, northeast, and
453 non-monsoon periods, with respective rates of change of $-0.94 \text{‰}/\text{‰}$ ($r = -0.49$), -

454 0.69 ‰/‰ ($r = -0.54$), and -0.65 ‰/‰ ($r = -0.44$). Similar patterns are detected for
 455 temperature–d-excess and specific humidity–d-excess correlations, showing gradual
 456 increases in the slopes and intercepts of the water vapor line. Moreover, the
 457 concentrated distribution of vapor values during the southwest monsoon and the highly
 458 scattered distribution during the northeast monsoon are indicative of the corresponding
 459 seasonal distributions of the water vapor line.



460
 461 **Figure 3: (a) Co-variation of water vapor isotopic composition and meteorological parameters**
 462 **during different monsoon and non-monsoon periods between March 1, 2020 and February 28,**
 463 **2021. The lines represent linear least-squares regressions (LMWL and GMWL) of δD (‰) as**
 464 **a function of $\delta^{18}\text{O}$ (‰). (b) Scatter plot of observed hourly water vapor isotopic $\delta^{18}\text{O}$ vs.**
 465 **specific humidity (q). The dashed red and blue curves represent the Rayleigh distillation line**
 466 **during the southwest and northeast monsoon. The solid black curve represents the mixing line.**
 467 **The colored curve represents the MBL-mixing line.**

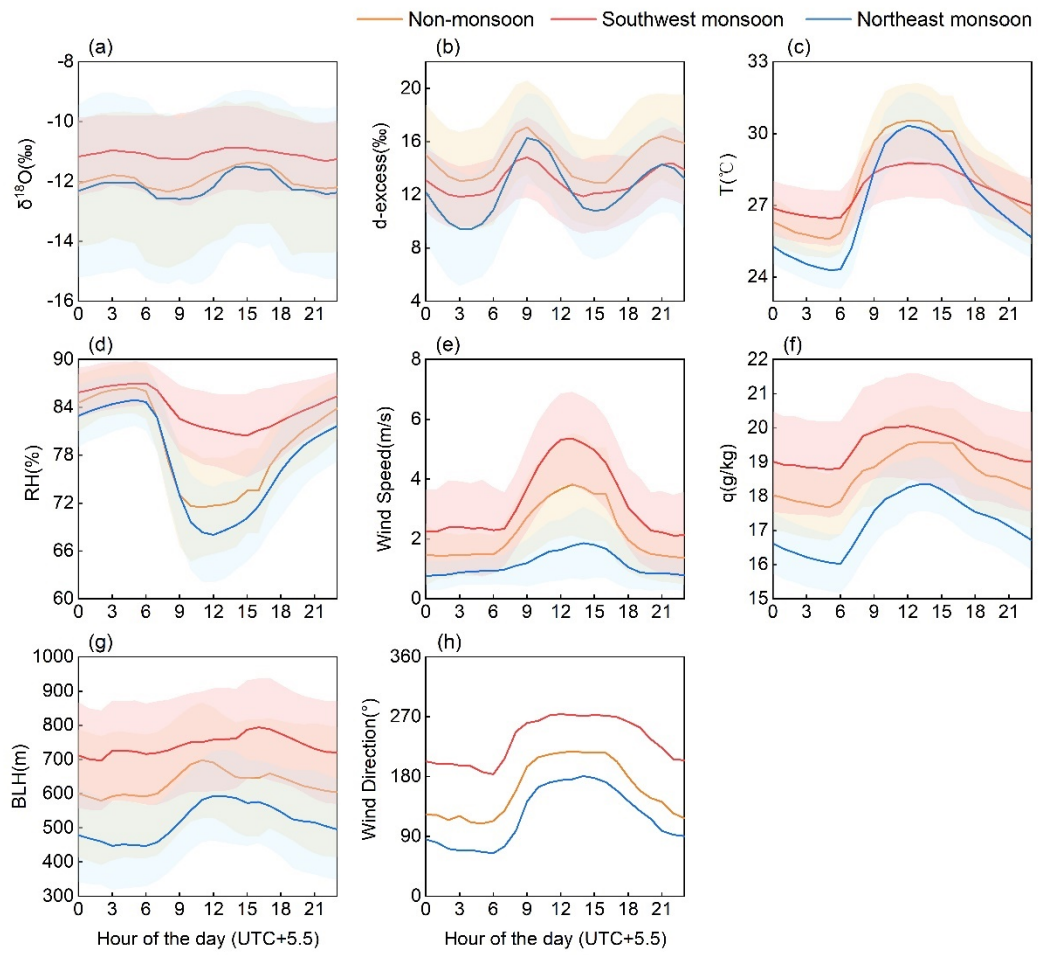
468 Plots of $q-\delta^{18}\text{O}$, the theoretical Rayleigh distillation curve, the mixing-line, and
 469 MBL-mixing curve, were used to assess mixing conditions during the study period (Fig.
 470 3b). During the southwest monsoon, most measurements are clustered between the
 471 Rayleigh and mixing curve, indicating isotopic variability dominated by effects of
 472 precipitation and moisture mixing process. Limited water vapor measurements are
 473 scattered below the Rayleigh fractionation line, implying a discernible impact of
 474 raindrop re-evaporation. Similarly, during the non-monsoon period, most
 475 measurements lie between the Rayleigh and mixing curves, with only a few located

476 below the Rayleigh line. During the northeast monsoon, $\delta^{18}\text{O}$ spans from the upper to
477 the lower extreme of the mixing and Rayleigh distillation curves. The measurements
478 substantially deviate from the Rayleigh curve and show a higher depletion than
479 predicted by the Rayleigh model, likely due to the influence of convective processes.

480 **3.2 The Variation Characteristics of Diurnal Cycles**

481 To look for diurnal cycles in isotopic composition and meteorological parameters,
482 we analyzed hourly averages (Fig. 4c-e). All isotopic ($\delta^{18}\text{O}$, δD , and d-excess) and
483 meteorological parameters exhibit strong diurnal variations during both monsoon and
484 non-monsoon periods (Fig. 4). Overall, the diurnal variations in local meteorological
485 parameters of solar radiation during the day and the resulting development of a
486 boundary layer led to the increasing of temperature and wind speed between the noon
487 and afternoon, accompanied by a decrease in relative humidity due to significant
488 evapotranspiration. At night, surface radiative cooling causes temperatures to drop,
489 resulting in calmer conditions near the surface and gradual air saturation, indicating a
490 relatively stable atmospheric boundary layer. During the southwest monsoon, $\delta^{18}\text{O}$, δD ,
491 relative humidity, wind speed, specific humidity, and BLH are generally higher than
492 during the northeast and non-monsoon periods, while d-excess is lower. In the early
493 morning, $\delta^{18}\text{O}$ steadily decreases, reaching a minimum (-11.26‰) around sunrise
494 (~09:00 local time (LT)). Subsequently, it increases throughout the day, peaking (-
495 10.87‰) in the afternoon (~15:00 LT), yielding a diurnal fluctuation of merely 0.45‰.
496 Increased specific humidity between 10:00 LT and 14:00 LT coincides with increasing
497 air temperatures and wind speeds and decreasing relative humidity (Fig. 4c-f). BLH
498 peaks between 14:00 LT and 16:00 LT, slightly later than other meteorological
499 parameters. The same diurnal variations for each parameter were observed during the
500 northeast monsoon, with maximum changes in $\delta^{18}\text{O}$ and d-excess of 1.1‰ and 6.8‰,
501 respectively. Specific humidity peaks between 10:00 LT and 16:00 LT, accompanied by
502 increases in air temperature, wind speed, and BLH. After 16:00 LT, specific humidity
503 decreases alongside isotopic δ values and other meteorological parameters. d-excess
504 peaks (14.81‰) at 09:00 LT and fluctuates until 23:00 LT, contrasting with the period

505 from 04:00 LT to 09:00 LT (Fig. 4b). d-excess exhibits a W-shaped variability, reaching
 506 similar highs at 09:00 LT and 21:00 LT. Specific humidity exhibits a diurnal variation
 507 that aligns closely with the $\delta^{18}\text{O}$ pattern, reaching its minimum before sunrise and
 508 peaking around midday (10:00-15:00 LT). Between afternoon and evening, specific
 509 humidity remains relatively high and stable. The diurnal variation during the southwest
 510 and northeast monsoon periods are 1.28 g/kg and 2.32 g/kg, respectively. Similarities
 511 with patterns observed at Lena River station in the eastern Siberia (Bonne et al. 2020)
 512 suggest potential influences from moisture exchange between the atmosphere and
 513 ocean surface, particularly during the northeast monsoon.



514

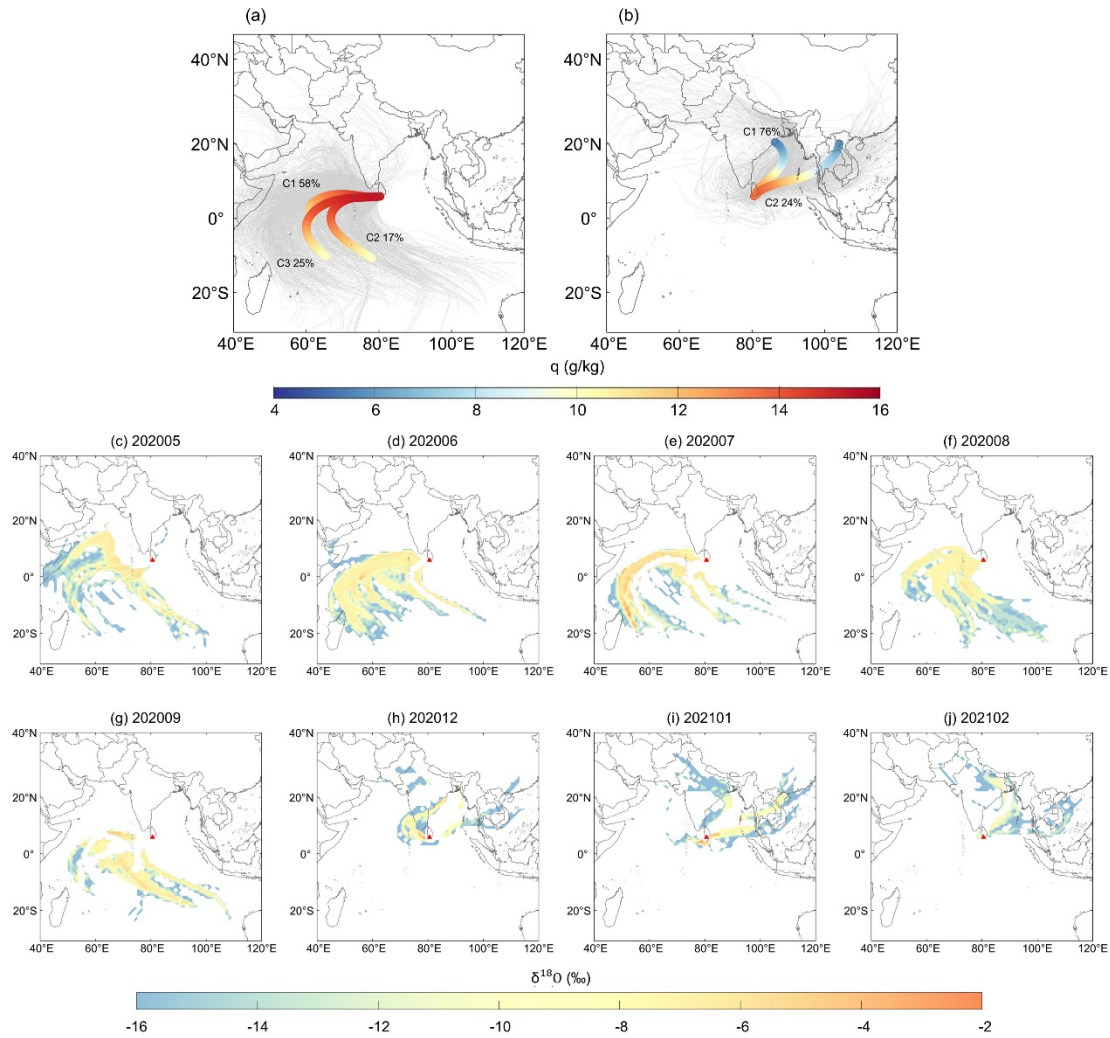
515 **Figure 4: Average diurnal cycles of (a) $\delta^{18}\text{O}$, (b) d-excess, (c) temperature (T), (d) relative**
 516 **humidity (RH), (e) wind speed, (f) specific humidity (q), (g) atmospheric boundary layer**
 517 **height (BLH), and (h) wind direction during the non-monsoon, southwest monsoon, and**
 518 **northeast monsoon periods. Shaded areas correspond to ± 1 standard deviation.**

519 **3.3 Sea Surface Evaporation Conditions in the Moisture Source**
520 **Region**

521 To be able to explore water vapor isotopic variations in the sea surface boundary
522 layer, we must first understand the processes and factors that affect isotope variations
523 during ocean surface water evaporation. The primary determinant governing water
524 vapor stable isotope shifts across different regions is the regional moisture transport
525 process, characterized by differences in isotopic variations in the moisture source
526 region, variations in meteorological conditions during the evaporation processes, and
527 divergences of the moisture transport pathways (Bonne et al., 2020). Thus, this section
528 aims to identify factors that drive the seasonal variations of near-surface atmospheric
529 water vapor stable isotopes at Matara, including water vapor origin, transmission routes,
530 and sea surface evaporation conditions in the source regions.

531 To further understand the different seasonal relationships between $\delta^{18}\text{O}$, d-excess,
532 and meteorological parameters, we analyzed potential seasonal differences between the
533 main moisture sources using HYSPLIT. Backward trajectories from the southwest and
534 northeast monsoons were spatially clustered and analyzed for changes in air mass
535 heights and specific humidity (Fig. S6), facilitating the identification of air mass origins.
536 The specific humidity along the path have been gridded, and we define the end points
537 of trajectories as the indicative of the moisture sources. Trajectories that reach Matara
538 during the southwest and northeast monsoons have different origins. During the
539 southwest monsoon, wind directions span from 60° to 360° and the main origin regions
540 are therefore the Arabian Sea (AS) and Indian Ocean (Fig. 5a). Due to the northward
541 movement of the warm South Equatorial Current, these winds gather significant
542 amounts of moisture along the way, bringing heavy rainfall to Matara (Fig. 5a and 5b).
543 Conversely, during the northeast monsoon, the main wind direction shifts to 0°-225°
544 and 330°-360°, such that most trajectories originate in northeast India, where specific
545 humidity is lower (overland), and only a short portion of the trajectory passes over the
546 BoB. The long transport distance results in a greater depletion in water vapor isotopes
547 once the air mass arrives at Matara station.

548 Moisture from all sources shows seasonal variations, with $\delta^{18}\text{O}$ values higher
 549 during the southwest monsoon than during the northeast monsoon. The shift in water
 550 vapor source from the AS in May to the southern Indian Ocean in September leads to
 551 $\delta^{18}\text{O}$ enriched water vapor from August to September. Enhanced convective activity
 552 and rainfall during the southwest monsoon result in $\delta^{18}\text{O}$ depletion, while tropical
 553 storms and hurricanes also contribute to $\delta^{18}\text{O}$ depletion.

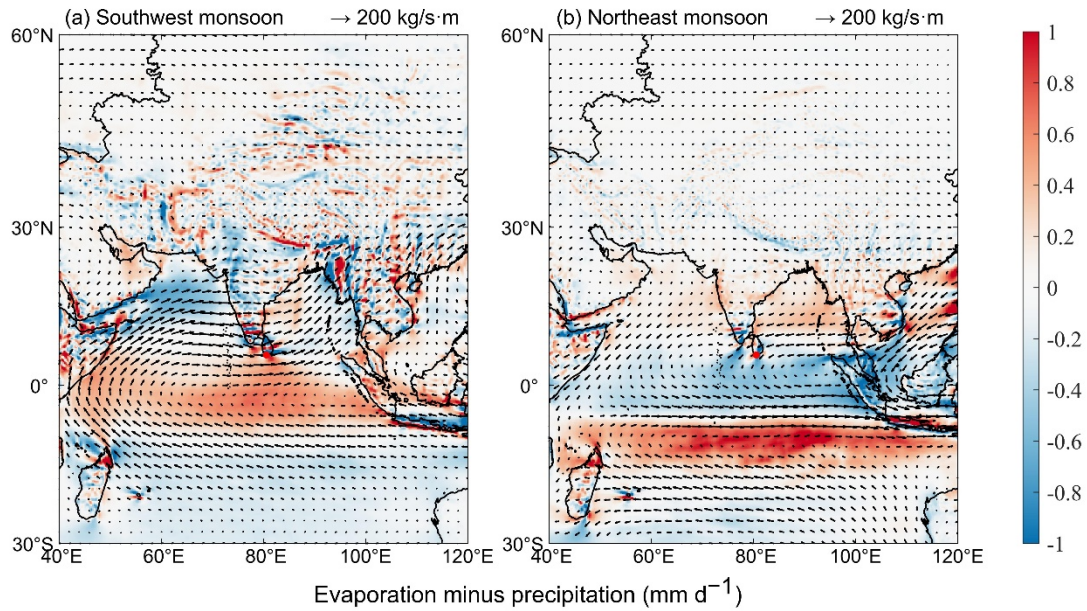


554 **Figure 5: Backward trajectories of water vapor tracks reaching Matara station and its four**
 555 **surrounding sites (heights: 50m, 500m, 1200m, and 2000m) during the (a) southwest monsoon**
 556 **and (b) northeast monsoon. The changes in specific humidity (q) along each clustered**
 557 **trajectory are shown in color. Numbers indicate the proportion (%) of trajectories represented**
 558 **by each clustered trajectory. Monthly concentration fields of water vapor isotopic $\delta^{18}\text{O}$ from**
 559 **a 168h HYSPLIT simulation of back trajectories during the two monsoon seasons (c-j). Red**

561 triangle marks the study site.

562 To assess how seasonal shifts in moisture sources impact the isotopic composition
563 of water vapor, we analyzed the relationship between specific humidity, isotope
564 variations, and wind direction at Matara station (Fig. S7). During the southwest
565 monsoon, wind directions were predominantly WNW, correlating with peak specific
566 humidity and highest $\delta^{18}\text{O}$ values and lowest d-excess, suggesting a westerly moisture
567 source. Conversely, air masses from the east exhibited $\delta^{18}\text{O}$ depletion and higher d-
568 excess. The northeast monsoon brought drier air from the BoB, leading to specific
569 humidity between 14 and 17 g/kg and significantly depleted $\delta^{18}\text{O}$ values. These air
570 masses likely experienced substantial isotopic fractionation during their overland
571 passage.

572 We also investigated the influence of water vapor flux, evaporation, and
573 precipitation on isotopic variations. The southwest monsoon saw lower evaporation
574 rates compared to precipitation at Matara station, contrasting with the northern Indian
575 Ocean and western BoB where evaporation surpassed precipitation. The northeast
576 monsoon, influenced by moisture from the BoB and South Asia, showed higher
577 evaporation rates, increasing water vapor flux. Overall, the water vapor flux and budget
578 varied markedly between monsoons, with the upstream vapor budget significantly
579 affecting stable isotope changes, particularly $\delta^{18}\text{O}$. The southwest monsoon's increased
580 precipitation and moisture transport from the northeast led to enriched $\delta^{18}\text{O}$ at Matara.
581 In contrast, the northeast monsoon's moisture transport resulted in a "washing effect",
582 causing a gradual $\delta^{18}\text{O}$ depletion due to continuous condensation and fractionation
583 along the transport pathway (Fig. 6 and S8).



584

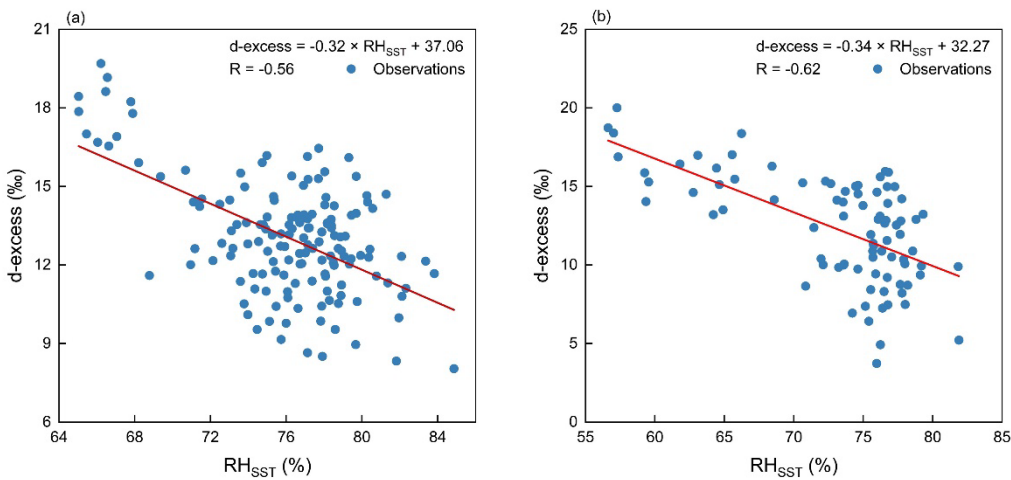
585 **Figure 6: Average water vapor flux and budget during the (a) southwest monsoon and (b)**
 586 **northeast monsoon, with the red dot marking Matara station.**

587 d-excess exhibits similar seasonal variations at Matara station, with lower values
 588 during the two monsoon seasons and higher values during the non-monsoon periods
 589 (Table 2, Fig. 4). This seasonal variation may stem from changes in relative humidity
 590 in the moisture source areas and further modifications during transport.

591 Ocean evaporation represents the starting point of the phase transformations that
 592 occur within the global water cycle. Identifying the isotopic variations and controlling
 593 factors of oceanic evaporation is essential for understanding isotopic shifts in the
 594 marine boundary layer. Previous coastal observational studies focusing on the marine
 595 boundary layer have confirmed a significant association between d-excess and RH_{SST}
 596 (Pfahl and Wernli, 2009; Steen-Larsen et al., 2015). In cases where kinetic fractionation
 597 during air mass transport is either absent or minimal, d-excess can serve as an indicator
 598 of the moisture source region (Bonne et al., 2014).

599 The map of the moisture sources (Fig. 5) identified the Indian Ocean and BoB as
 600 the main source areas for moisture arriving at Matara station. To gauge the impact of
 601 more local influences, we investigated how changes in sea surface meteorological
 602 conditions in the sea around Matara station affects near surface water vapor isotope
 603 concentrations (Fig. S9). During the southwest monsoon, RH_{SST} in "Region a" (located

604 to the south of Matara between 3-7°N and 56-65°E) ranged from 64% to 86%, with
 605 SST fluctuating between 27.9°C and 31.5°C. During the northeast monsoon, RH_{SST} in
 606 "Region b" (located to the east of Matara between 6-8°N and 82-85°E) ranged from 54%
 607 to 84%, with SST fluctuating between 28.1°C and 29.1°C. In comparison with the
 608 southwest monsoon, RH_{SST} is slightly lower, accompanied by less pronounced
 609 variability in SST. The rate of change in d-excess under the influence of RH_{SST} in the
 610 BoB (during the northeast monsoon) is -0.34 ‰/%. In comparison, the rate of change
 611 in d-excess with the RH_{SST} of the northern Indian Ocean (during the southwest monsoon)
 612 is -0.32 ‰/%, suggesting that evaporation over the northern Indian Ocean significantly
 613 impacts local d-excess. Studies focused on the BoB's sea surface revealed that RH_{SST}
 614 explains only 25% of the d-excess variation ($d\text{-excess} = (-0.55 \pm 0.14) \times RH_{SST} + (56 \pm 12)$;
 615 $r = -0.5$). The limited variation in relative humidity during the monsoon period
 616 led to a low correlation, indicating that monsoon moisture plays a crucial role in the
 617 isotopic composition of water vapor in the BoB (Midhun et al., 2013). Conversely, the
 618 observed relationship between near-surface water vapor d-excess at Matara and relative
 619 humidity in the surrounding oceanic region during the observational period, with
 620 correlation coefficients of -0.56 and -0.62 ($p < 0.01$), respectively (Fig. 7), reveals a
 621 marked negative correlation between d-excess and relative humidity in the nearby
 622 Indian Ocean and BoB, indicating that water vapor at Matara is predominantly supplied
 623 by nearby oceans. Notably, SST amplitude near the Matara station is smaller than the
 624 variations in near-surface air temperature (Fig. 2).



625

626 **Figure 7: Relationship between d-excess and RH_{SST} during the (a) southwest monsoon and (b)**
627 **northeast monsoon. Specific sea regions (Fig. S10) to the south (Region a: 3-7°N and 56-65°E)**
628 **and east (Region b: 6-8°N and 82-85°E) of the observation station were selected to investigate**
629 **the impact of sea surface meteorological conditions on near-surface water vapor isotopes**
630 **during the two monsoon periods.**

631 **3.4 The Influence of Regional Convective Activity**

632 In the equatorial tropics, OLR mainly results from convective activity and cloud
633 cover, which can impact the stable isotope composition of precipitation (Ohring et al.,
634 1984; Gao et al., 2013; Guo et al., 2017). Generally, higher OLR values are associated
635 with weaker convective activity. Examining the correlation between stable isotopes of
636 water vapor and OLR helps to understand the impact of convective activities along
637 near-surface trajectories of water vapor stable isotopes at Matara station.

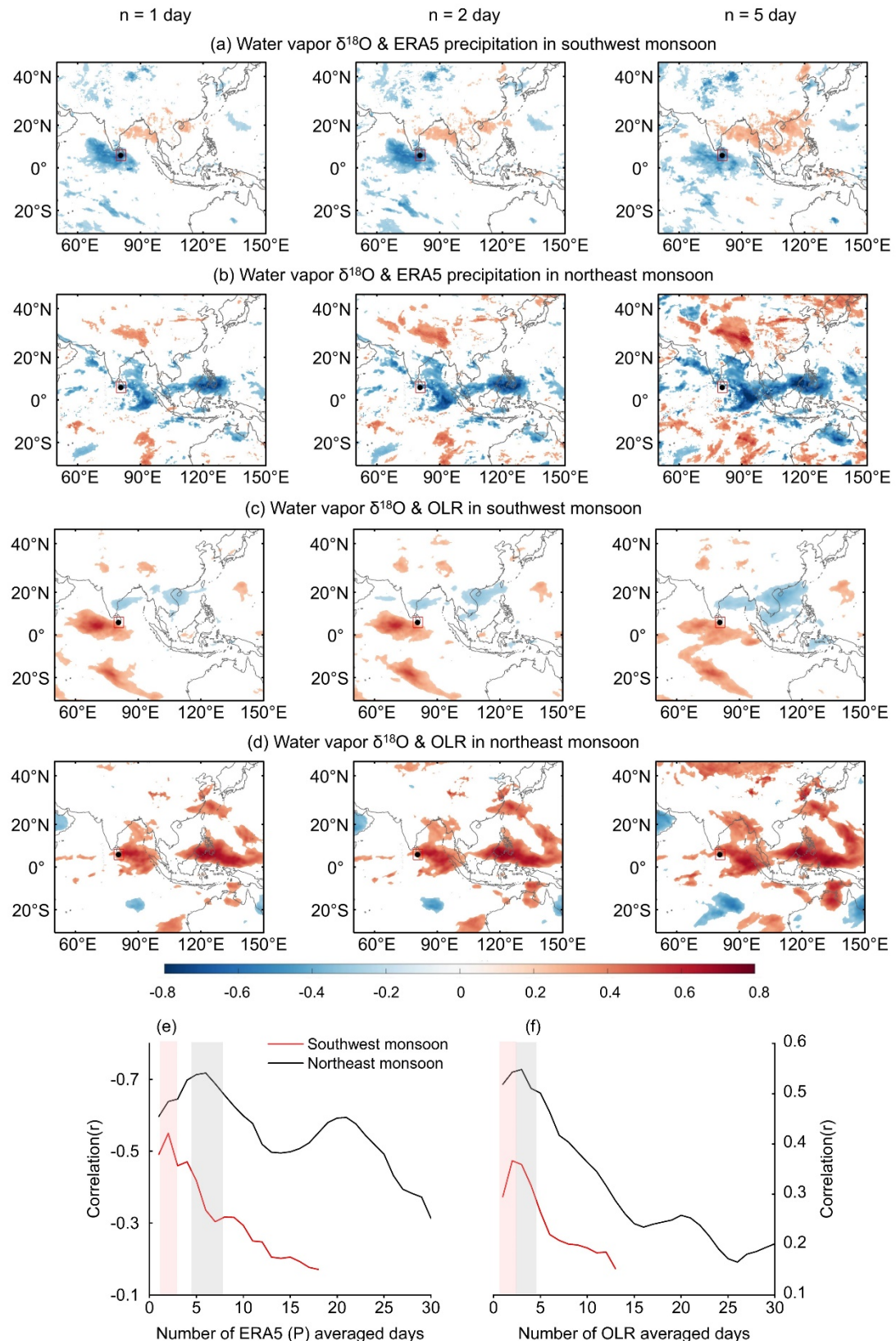
638 We calculated the spatiotemporal correlation between OLR and precipitation
639 amount using the measured water vapor isotopic compositions at Matara station.
640 Specifically, we calculated the average precipitation amount and average OLR for each
641 grid point by averaging over different numbers of days ($n = 1, 2$, up to 30) preceding
642 each day. Lower OLR values indicate the presence of deep convective clouds in this
643 region and higher precipitation associated with lower δ values.

644 Fig. 8a shows the strong positive correlation (red regions) between rainfall and
645 $\delta^{18}\text{O}$ during the southwest monsoon, mainly in the northern BoB and over India. This
646 correlation strengthens and extends over wider areas as n increases from 1 to 5.
647 Additionally, a strong negative correlation is evident in the northern Indian Ocean and
648 southern Arabian Sea, reaching a maximum for $n = 2$ d. During the northeast monsoon,
649 the spatial correlation distribution differs, with a negative correlation observed over the
650 southern Indian Ocean and BoB (Fig. 8b), reaching a maximum for $n = 5$ d. Lower OLR
651 values in the Arabian Sea and the northern part of the India Ocean correspond to a
652 decrease in water vapor isotopic $\delta^{18}\text{O}$ at Matara station (Fig. 8c, d). This pattern
653 indicates that water vapor $\delta^{18}\text{O}$ during the northeast monsoon period is influenced by
654 convective activities over the South BoB, and Southeast Asian regions. The stronger

655 this convective activity, the more depleted is the air reaching Matara in water vapor
656 isotopic $\delta^{18}\text{O}$.

657 To examine the correlation between water vapor isotopic $\delta^{18}\text{O}$ and local
658 precipitation (Fig. 8e) and OLR (Fig. 8f), we selected a small region of $5^\circ \times 5^\circ$ around
659 Matara and calculated the temporal correlation for all grid points as described above.
660 The results show that the correlation with precipitation is negative during both monsoon
661 seasons as expected. The depletion of low-level water vapor $\delta^{18}\text{O}$ is related to the
662 transport and deposition of water vapor into the lower atmosphere through convective
663 activity (Kurita, 2013; Midhun et al., 2013; Lekshmy et al., 2014). The air masses are
664 re-supplied to the convective system through moisture recycling. This results in a strong
665 correlation between the isotopic composition of water vapor and the convective activity
666 during the previous day (Fig. 8f). Residual water vapor is more depleted in strong
667 convective systems. In our study, the correlation reaches a high value after about 5 days,
668 indicating that the convective activity is sufficiently established to affect the isotopic
669 composition of water vapor. In fact, the correlation (for $p < 0.05$ and in absolute terms)
670 is high for all n values, with maxima of about 0.37 for $n = 2$ d during the southwest
671 monsoon and 0.55 for $n = 2$ to 5 d during the northeast monsoon.

672 The OLR correlation peaks at smaller time scales (approximately $n = 2$ -5 d, Fig.
673 8f) than precipitation ($n = 3$ -7 d). We attribute this difference to the effect of cloud
674 distribution on precipitation and OLR. OLR has a stronger response to shallow clouds,
675 while precipitation is more responsive to both deep convective clouds and shallow
676 clouds (Masunaga and Kummerow, 2006; Schumacher, 2006). The OLR minimum
677 occurs when thunderstorm clouds result in more precipitation. Additionally, deep
678 thunderstorm clouds, with short lifetimes and consequently very low OLR
679 (corresponding to highly depleted water vapor isotopic δ), exhibit a short memory effect
680 on the correlation (peak occurs at smaller time scales) (Gambheer and Bhat, 2000).



681

682

683

881

Figure 8: Isotopic composition correlations with precipitation and OLR during monsoon periods. (a, b): Spatial correlations between water vapor $\delta^{18}\text{O}$ and ERA5-precipitation for the southwest (a) and northeast (b) monsoons. (c, d): Spatial correlations between water vapor

685 **$\delta^{18}\text{O}$ and average OLR for the southwest (c) and northeast (d) monsoons. (e): Correlation**
686 **between $\delta^{18}\text{O}$ and ERA5-precipitation (P) across different averaging periods (n = 1 to 30 days)**
687 **for southwest (red line) and northeast (black line) monsoons. (f): Correlation between $\delta^{18}\text{O}$**
688 **and OLR across southwest (red line) and northeast (black line) monsoons over varying**
689 **averaging periods. Red areas indicate significant negative correlations, grey areas indicate**
690 **significant positive correlations.**

691 **Note: Only correlations surpassing the 99% confidence threshold are displayed. The red box**
692 **denotes the Matara station's region of interest.**

693

694 **4. Discussion: Comparing Main Features and Identifying Influencing**
695 **Factors**

696 This study presented the results from a one-year (March 2020 to February 2021)
697 in-situ measurement campaign of near-surface atmospheric water vapor isotopes ($\delta^{18}\text{O}$,
698 δD) at Matara station, Sri Lanka. These high-temporal resolution water vapor isotopic
699 composition and meteorological observations provided a good opportunity to
700 investigate the water vapor isotopic dynamics from synoptic to seasonal scales. The
701 variability of water vapor isotopes at Matara station is influenced by local
702 meteorological factors, oceanic evaporation processes, and regional convective
703 activities, depending on the water sources and moisture transport. The measurements
704 provided insights into multi-time-scale variations in near-surface atmospheric water
705 vapor in an equatorial region and provided information about the interactions between
706 large-scale atmospheric moisture transport and oceanic evaporation.

707 During the both monsoon periods, specific humidity and stable water isotope
708 composition showed a clear diurnal cycle at Matara station, primarily due to the
709 significant contribution of local evapotranspiration to the overall moisture balance. In
710 equatorial regions, seasonal variations in stable water vapor isotopes are largely
711 governed by changes moisture sources and the transport processes. Ponmudi station,
712 located in southern India (Lekshmy et al., 2018), shares many characteristics with
713 Matara station, in that it is also a coastal city, influenced by both the southwest and

714 northeast monsoons. During the summer, moisture sources for air arriving at Ponmudi
715 are mostly located in the southern Arabian Sea and equatorial Indian Ocean, with
716 relative humidity levels exceeding 70%. This high relative humidity, combined with a
717 continuous supply of moisture from the Arabian Sea, results in significant rainfall in
718 the Ponmudi region, exceeding 2040 mm per year.

719 Fluctuations of water vapor stable isotopes at shorter (weather) time scales are
720 closely associated with regional convective activities. Research conducted on
721 precipitation and water vapor stable isotopes at Bangalore, another coastal city in
722 southern India, indicates that local meteorological parameters do not influence isotope
723 ratios (Rahul et al., 2016b). Rather, these ratios are affected by the integrated regional
724 convective activity, characterized by large-scale rainfall or outgoing longwave radiation
725 flux. Like Matara station, Bangalore is also affected by both the southwest and northeast
726 monsoons. The observed depletion in heavy isotopes may be due to the influx of
727 moisture from the Bay of Bengal, depleted due to the rainout effect, mixing with air
728 that has travelled overland crossing the Indian subcontinent.

729 Overall, the long-term monitoring of water vapor stable isotopes in South Asian
730 equatorial regions could highlight the importance of both seasonal and sub-seasonal
731 (weather-scale) variations, mostly due to changes in moisture sources and processes
732 that occur during the air mass transport at the circulation scale. Matara station served
733 as a good location to study the effects of moisture transport processes over the Indian
734 Ocean. We could also identify seasonal patterns that in general agree with previous
735 findings for tropical equatorial regions (Midhun et al., 2013; Rahul et al., 2016b;
736 Lekshmy et al., 2018).

737

738 **5. Summary and Conclusions**

739 One-year (March 2020 to February 2021) in situ meteorological observations and
740 measurements of water vapor isotopic composition were conducted at Matara station,
741 Sri Lanka. Meteorological parameters exhibited diurnal variations during both
742 monsoon and non-monsoon periods. The new dataset provides detailed information on

743 the isotopic composition of near-surface atmospheric water vapor, which complements
744 local precipitation isotopic dataset by including periods without rainfall. Additionally,
745 it enables a comparative analysis of water vapor isotopic variations across the two
746 monsoon periods. Research findings indicate that during the northeast monsoon, diurnal
747 fluctuations in $\delta^{18}\text{O}$, temperature, and specific humidity were observed, with maximum
748 values reaching 1.1‰, 6.0°C, and 2.3 g/kg, respectively. In contrast, during the
749 southwest monsoon these parameters exhibit only small magnitude fluctuations of
750 0.45‰, 2.3°C, and 1.3 g/kg. Atmospheric temperature affects isotopic composition
751 through its effect on isotope fractionation. Additionally, a weak seasonal variability in
752 near-surface water vapor isotopes was observed, with $\delta^{18}\text{O}$ typically showing high
753 values (-11.1‰) during the monsoon period and low values (-11.9‰) during the non-
754 monsoon period. d-excess exhibited lower value (12.7‰) during the monsoon period
755 than during the non-monsoon period (14.7‰).

756 An evaluation of water vapor sources using HYSPLIT indicates small but notable
757 seasonal variations in air mass origins. The source regions differ seasonally, with the
758 northern Indian Ocean serving as the primary source during the southwest monsoon,
759 and the Bay of Bengal dominating as the source during the northeast monsoon.
760 Significant variations in water vapor flux and budget occur during the monsoon periods,
761 with upstream water vapor budgets exerting a pronounced impact on isotopic signatures,
762 especially $\delta^{18}\text{O}$. Evaporation over the northern Indian Ocean significantly impacts local
763 d-excess at Matara. Contrary to previous research indicating a weak correlation ($r = -$
764 0.5) between d-excess in the Bay of Bengal and the sea surface relative humidity (RH_{SST})
765 (Midhun et al., 2013), we found a slightly stronger negative correlation with RH_{SST}
766 during the monsoon periods, with values of -0.61 and -0.62 ($p < 0.01$) for the northern
767 Indian Ocean and Bay of Bengal, respectively. This study underscores the capability of
768 near-surface d-excess to reflect the evaporation conditions over these oceanic source
769 regions. However, the impact of raindrop evaporation is yet to be thoroughly explored.

770 Consistent with previous research (Rahul et al., 2016b), large-scale rainfall and
771 regional convective activity (OLR) significantly impact isotope ratios at Matara station.

772 Notably, significant changes in $\delta^{18}\text{O}$ were observed during a heavy rainfall event in July
773 2020, with a sharp decline in isotopic values from $-10.4\text{\textperthousand}$ to $-20.4\text{\textperthousand}$ within 20 hours.
774 During the southwest monsoon, strong cloud cover and high humidity over the ocean
775 may lead to $\delta^{18}\text{O}$ enrichment at Matara station. The water vapor isotope compositions
776 observed during the southwest monsoon are similar as those observed in the Bay of
777 Bengal (Midhun et al., 2013). The depleted of water vapor isotope values at Matara
778 station in autumn and winter is consistent with findings from other coastal stations, such
779 as Bangalore, Ponmudi, and Wayanad (Rahul et al., 2016b; Lekshmy et al., 2018).
780 Current investigations into convection activities and evaporation processes in tropical
781 and subtropical regions offer fresh perspectives on the stable isotopic composition of
782 water vapor in these regions (Landshuter et al., 2024; Galewsky et al., 2023; Baily et
783 al., 2015). The re-evaporation of raindrops in deep convection (Risi et al., 2019) and
784 the formation of ice clouds in tropical regions (de Vries et al., 2022), which influence
785 the tropopause, provide critical insights into the factors governing isotopic variability
786 during shallow and deep convection. Simulations that incorporate entrainment and
787 mixing processes highlight the importance of accurately quantifying the effects of
788 hydrometeor evaporation on water vapor stable isotopes (Risi et al., 2019; Benetti et al.,
789 2015). These findings form a basis for deeper exploration of the distinctive isotopic
790 characteristics of tropical water vapor during the different monsoon periods. Our study
791 is the first to point out that the correlation between OLR and $\delta^{18}\text{O}$ peaks around 2-5
792 days before the observation, which we attribute to the impacts of cloud distribution.

793 This study examines the origins of moisture arriving at Matara station and the
794 associated atmospheric transport, with a focus on the substantial impact of cloud
795 distribution on the stable isotopic composition of water vapor, driven by regional
796 convection. Therefore, these insights are crucial for refining our grasp of isotopic
797 dynamics, particularly in relation to cloud microphysics and atmospheric mixing
798 processes within the broader water cycle (de Vries et al., 2022). This comprehensive
799 dataset containing synchronous water vapor isotope and meteorological measurements
800 offer extensive opportunities for further analyses, e.g., of the typical weather events,

801 atmospheric patterns, and ocean-atmosphere interactions in the equatorial region.
802 Given that only one year of observations is currently available, there is a pressing need
803 for supplementary and sustained measurements of water vapor stable isotopes in this
804 region to support multi-year studies and interannual variabilities. Furthermore, given
805 the anticipated changes in numerous weather and hydrological processes in equatorial
806 regions, future research should explore the impacts of typical weather events, and
807 ocean-atmosphere interactions, to deepen our understanding of extreme events and
808 large-scale atmospheric modes (e.g., ENSO, MJO, and IOD). Considering the temporal
809 and spatial variability in the dynamics of tropical ocean-atmosphere systems, high-
810 resolution isotope models and satellite datasets should be combined for a more
811 comprehensive analysis in the future.

812 **Acknowledgements:**

813 This work was funded by The Second Tibetan Plateau Scientific Expedition and
814 Research (STEP) program (Grant No. 2019QZKK0208) and the National Natural
815 Science Foundation of China (Grants 41922002 and 41988101-03), as well as the
816 Innovation Program for Young Scholars of TPESER (QNCX2022ZD-01). We thank
817 staff in the China Sri Lanka Joint Center for Education and Research, Mr. Charith
818 Madusanka Widanage, and Dr. Di Dai for their invaluable support and assistance with
819 measurements.

820

821 **Author Contributions:**

822 **WYQ:** Data curation, Formal analysis, Writing - Original draft preparation. **GJ:**
823 Data curation, Conceptualization, Methodology, Supervision, Writing - Review and
824 Editing, Funding acquisition. **ZAB:** Writing - Review and Editing, Project
825 administration. **NXW:** Data curation. **LYG:** Data curation. **RD:** Project administration.
826 **GTP:** Project administration. **SAHR:** Data curation.

827

828 **Data availability:**

829 The ERA5 dataset is the latest reanalysis dataset published by the European Centre
830 for Medium-Range Weather Forecasts (ECMWF) (Hersbach et al., 2020)
831 (<https://cds.climate.copernicus.eu/cdsapp#!/home>). The Global Data Assimilation
832 System (GDAS) has been published by the US National Oceanic and Atmospheric
833 Administration (NOAA) (<ftp://arlftp.arlhq.noaa.gov/archives/gdas1/>). The water vapor
834 isotopic compositions dataset will be available on the Zenodo research data repository
835 after manuscript publication.

836

837 **Competing interests:**

838 The contact author has declared that none of the authors has any competing interests.

839 **References**

840 Aemisegger, F., and Sjolte, J.: A Climatology of Strong Large-Scale Ocean Evaporation
841 Events. Part II: Relevance for the Deuterium Excess Signature of the
842 Evaporation Flux, *J. Climate*, 31, 7313-7336, <https://doi.org/10.1175/JCLI-D-17-0592.1>, 2018.

843

844 Aemisegger, F., Sturm, P., Graf, P., Sodemann, H., Pfahl, S., Knohl, A., and Wernli, H.:
845 Measuring variations of $\delta^{18}\text{O}$ and $\delta^2\text{H}$ in atmospheric water vapour using two
846 commercial laser-based spectrometers: an instrument characterisation study,
847 *Atmos. Meas. Tech.*, 5, 1491-1511, <https://doi.org/10.5194/amt-5-1491-2012>,
848 2012.

849 Angert, A., Lee, J.E., and Yakir, D.: Seasonal variations in the isotopic composition of
850 near-surface water vapour in the eastern Mediterranean, *Tellus B*, 60, 674-684,
851 <https://doi.org/10.1111/j.1600-0889.2008.00357.x>, 2008.

852 Bailey, A., Aemisegger, F., Villiger, L., Los, S.A., Reverdin, G., Quiñones Meléndez,
853 E., Acquistapace, C., Baranowski, D.B., Böck, T., Bony, S., Bordsdorff, T.,
854 Coffman, D., de Szoke, S.P., Diekmann, C.J., Dütsch, M., Ertl, B., Galewsky,
855 J., Henze, D., Makuch, P., Noone, D., Quinn, P.K., Rösch, M., Schneider, A.,
856 Schneider, M., Speich, S., Stevens, B., and Thompson, E.J.: Isotopic
857 measurements in water vapor, precipitation, and seawater during EUREC4A,
858 *Earth Syst. Sci. Data*, 15, 465-495, <https://doi.org/10.5194/essd-15-465-2023>,
859 2023.

860 Bailey, H.L., Kaufman, D.S., Henderson, A.C.G., Leng, M.J.: Synoptic scale controls
861 on the $\delta^{18}\text{O}$ in precipitation across Beringia, *Geophys. Res. Lett.*, 42, 4608-
862 4616, <https://doi.org/10.1002/2015GL063983>, 2015.

863 Bandara, U., Agarwal, A., Srinivasan, G., Shanmugasundaram, J., and Jayawardena,
864 I.M.S.: Intercomparison of gridded precipitation datasets for prospective
865 hydrological applications in Sri Lanka, *Int. J. Climatol.*, 42, 3378-3396,
866 <https://doi.org/10.1002/joc.7421>, 2022.

867 Bavadekar, S.N., and Mooley, D.A.: Use of the equation of continuity of water vapour

868 for computation of average precipitation over peninsular India during the
869 summer monsoon, In: Lighthill, J., Pearce, P.R. (Eds.), *Monsoon Dynamics*,
870 Cambridge University Press, Cambridge, pp., 261-268, 1981.

871 Bedaso, Z., and Wu, S-Y.: Daily precipitation isotope variation in Midwestern United
872 States: Implication for hydroclimate and moisture source, *Sci. Total Environ.*,
873 713, 136631, <https://doi.org/10.1016/j.scitotenv.2020.136631>, 2020.

874 Benetti, M., Aloisi, G., Reverdin, G., Risi, C., and Sèze, G.: Importance of boundary
875 layer mixing for the isotopic composition of surface vapor over the subtropical
876 North Atlantic Ocean, *J. Geophys. Res. Atmos.*, 120, 2190-2209,
877 <https://doi.org/10.1002/2014JD021947>, 2015.

878 Benetti, M., Lacour, J-L., Sveinbjörnsdóttir, A.E., Aloisi, G., Reverdin, G., Risi, C.,
879 Peters, A.J., and Steen-Larsen, H.C.: A Framework to Study Mixing Processes
880 in the Marine Boundary Layer Using Water Vapor Isotope Measurements,
881 *Geophys. Res. Lett.*, 45(5), 2524-2532, <https://doi.org/10.1002/2018GL077167>,
882 2018.

883 Benetti, M., Reverdin, G., Pierre, C., Merlivat, L., Risi, C., Steen-Larsen, H.C., and
884 Vimeux, F.: Deuterium excess in marine water vapor: Dependency on relative
885 humidity and surface wind speed during evaporation, *J. Geophys. Res. Atmos.*,
886 119, 584-593, <https://doi.org/10.1002/2013JD020535>, 2014.

887 Bhattacharya, S., Pal, M., Panda, B., and Pradhan, M.: Spectroscopic investigation of
888 hydrogen and triple-oxygen isotopes in atmospheric water vapor and
889 precipitation during Indian monsoon season, *Isot. Environ. Health. S.*, 57, 368-
890 385, <https://doi.org/10.1080/10256016.2021.1931169>, 2021.

891 Blossey, P.N., Kuang, Z., and Romps, D.M.: Isotopic composition of water in the
892 tropical tropopause layer in cloud-resolving simulations of an idealized tropical
893 circulation, *J. Geophys. Res. Atmos.*, 115, D24309, doi:
894 <https://doi.org/10.1029/2010JD014554>, 2010.

895 Bonne, J-L., Behrens, M., Meyer, H., Kipfstuhl, S., Rabe, B., Schönicke, L., Steen-
896 Larsen, H.C., and Werner, M.: Resolving the controls of water vapour isotopes

897 in the Atlantic sector, *Nat. Commun.*, 10, 1632, <https://doi.org/10.1038/s41467-019-09242-6>, 2019.

898

899 Bonne, J-L., Masson-Delmotte, V., Cattani, O., Delmotte, M., Risi, C., Sodemann, H.,
900 and Steen-Larsen, H.C.: The isotopic composition of water vapour and
901 precipitation in Ivittuut, Southern Greenland, *Atmos. Chem. Phys.*, 14, 4419-
902 2014, <https://doi.org/10.5194/acp-14-4419-2014>, 2014.

903 Bonne, J-L., Meyer, H., Behrens, M., Boike, J., Kipfstuhl, S., Rabe, B., Schmidt, T.,
904 Schönicke, L., Steen-Larsen, H.C., and Werner, M.: Moisture origin as a driver
905 of temporal variabilities of the water vapour isotopic composition in the Lena
906 River Delta, Siberia, *Atmos. Chem. Phys.*, 20, 10493-10511,
907 <https://doi.org/10.5194/acp-20-10493-2020>, 2020.

908 Bookhagen, B., and Burbank, D.W.: Toward a complete Himalayan hydrological
909 budget: Spatiotemporal distribution of snowmelt and rainfall and their impact
910 on river discharge, *J. Geophys. Res.*, 115, F03019,
911 <https://doi.org/10.1029/2009JF001426>, 2010.

912 Cai, Z., Tian, L., and Bowen, G.J.: ENSO variability reflected in precipitation oxygen
913 isotopes across the Asian Summer Monsoon region, *Earth Planet. Sci. Lett.*, 475,
914 25-33, <https://doi.org/10.1016/j.epsl.2017.06.035>, 2017.

915 Cai, Z., and Tian, L.: Atmospheric Controls on Seasonal and Interannual Variations in
916 the Precipitation Isotope in the East Asian Monsoon Region, *J. Climate*, 29,
917 1339-1352, <https://doi.org/10.1175/JCLI-D-15-0363.1>, 2016.

918 Chakraborty, S., Sinha, N., Chattopadhyay, R., Sengupta, S., Mohan, P.M., and Datye,
919 A.: Atmospheric controls on the precipitation isotopes over the Andaman
920 Islands, Bay of Bengal, *Sci. Rep.*, 6, 19555, <https://doi.org/10.1038/srep19555>,
921 2016.

922 Craig, H.: Isotopic Variation in Meteoric Waters. *Science*, 133, 1702-1703,
923 <https://doi.org/10.1126/science.133.3465.1702>, 1961.

924 Craig, H., and Gordon, L.I.: Deuterium and oxygen 18 variation in the ocean and the
925 marine atmosphere, In: Tongiorgi, E. (Eds.), *Stable Isotopes in Oceanographic*

926 Studies and Paleotemperatures, pp., 9-130, 1965.

927 Curry, J.A., and Webster, P.J.: Thermodynamics of Atmospheres and Oceans, Academic
928 Press, London, 31705, 1999.

929 Dai, D., Gao, J., Steen-Larsen, H.C., Yao, T., Ma, Y., Zhu, M., and Li, S.: Continuous
930 monitoring of the isotopic composition of surface water vapor at Lhasa,
931 southern Tibetan Plateau, Atmos. Res., 264, 105827,
932 <https://doi.org/10.1016/j.atmosres.2021.105827>, 2021.

933 Dansgaard, W.F.: Stable Isotopes in Precipitation, Tellus B, 16, 436-468,
934 <https://doi.org/10.1111/j.2153-3490.1964.tb00181.x>, 1964.

935 Delattre, H., Vallet-Coulomb, C., and Sonzogni, C.: Deuterium excess in the
936 atmospheric water vapour of a Mediterranean coastal wetland: regional vs. local
937 signatures, Atmos. Chem. Phys., 15, 10167-10181, <https://doi.org/10.5194/acp-15-10167-2015>, 2015.

939 de Vries, A.J., Aemisegger, F., Pfahl, S., and Wernli, H.: Stable water isotope signals in
940 tropical ice clouds in the West African monsoon simulated with a regional
941 convection-permitting model, Atmos. Chem. Phys., 22, 8863-8895,
942 <https://doi.org/10.5194/acp-22-8863-2022>, 2022.

943 Dhar, O., and Rakhecha, P.: Foreshadowing Northeast Monsoon Rainfall Over Tamil
944 Nadu, India, Mon. Weather Rev., 111, 109, [https://doi.org/10.1175/1520-0493\(1983\)111<0109:FNMROT>2.0.CO;2](https://doi.org/10.1175/1520-0493(1983)111<0109:FNMROT>2.0.CO;2), 1983.

946 Diekmann, C.J., Schneider, M., Knippertz, P., de Vries, A.J., Pfahl, S., Aemisegger, F.,
947 Dahinden, F., Ertl, B., Khosrawi, F., Wernli, H., and Braesicke, P.: A Lagrangian
948 Perspective on Stable Water Isotopes During the West African Monsoon, J.
949 Geophys. Res. Atmos., 126, e2021JD034895,
950 <https://doi.org/10.1029/2021JD034895>, 2021.

951 Dütsch, M., Pfahl, S., Meyer, M., and Wernli, H.: Lagrangian process attribution of
952 isotopic variations in near-surface water vapour in a 30-year regional climate
953 simulation over Europe, Atmos. Chem. Phys., 18, 1653-1669,
954 <https://doi.org/10.5194/acp-18-1653-2018>, 2018.

955 Gadgil, S.: The Indian Monsoon and Its Variability, Rev. Earth Pl. Sci., 31, 429-467,
956 <https://doi.org/10.1146/annurev.earth.31.100901.141251>, 2003.

957 Galewsky, J., and Hurley, J.V.: An advection-condensation model for subtropical water
958 vapor isotopic ratios, J. Geophys. Res. Atmos., 115, 116,
959 <https://doi.org/10.1029/2009JD013651>, 2010.

960 Galewsky, J., Schneider, M., Diekmann, C., Semie, A., Bony, S., Risi, C., Emanuel, K.,
961 Brogniez, H.: The Influence of Convective Aggregation on the Stable Isotopic
962 Composition of Water Vapor, AGU Advances, 4, e2023AV000877,
963 <https://doi.org/10.1029/2023AV000877>, 2023.

964 Galewsky, J., Steen-Larsen, H.C., Field, R.D., Worden, J., Risi, C., and Schneider, M.:
965 Stable isotopes in atmospheric water vapor and applications to the hydrologic
966 cycle, Rev. Geophy., 54, 809-865, <https://doi.org/10.1002/2015RG000512>,
967 2016.

968 Gambheer, A.V., and Bhat, G.S.: Life Cycle Characteristics of Deep Cloud Systems
969 over the Indian Region Using INSAT-1B Pixel Data, Mon. Weather Rev., 128,
970 4071-4083, [https://doi.org/10.1175/1520-0493\(2000\)129<4071:LCCODC>2.0.CO;2](https://doi.org/10.1175/1520-0493(2000)129<4071:LCCODC>2.0.CO;2), 2000.

972 Gao, J., Masson-Delmotte, V., Risi, C., He, Y., and Yao, T.: What controls precipitation
973 $\delta^{18}\text{O}$ in the southern Tibetan Plateau at seasonal and intra-seasonal scales? A
974 case study at Lhasa and Nyalam, Tellus B, 65, 21043,
975 <https://doi.org/10.3402/tellusb.v65i0.21043>, 2013.

976 Gao, Y., Li, X., Leung, L. R., Chen, D., and Xu, J.: Aridity changes in the Tibetan
977 Plateau in a warming climate, Environ. Res. Lett., 9, 104013,
978 <https://doi.org/10.1088/1748-9326/10/3/034013>, 2014.

979 Gat, J.: Oxygen and hydrogen isotopes in the hydrologic cycle, Annu. Rev. Earth Pl.
980 Sci., 24, 225-262, <https://doi.org/10.1146/ANNUREV.EARTH.24.1.225>, 1996.

981 Gedzelman, S., Lawrence, J., Gamache, J., Black, M., Hindman, E., Black, R., Dunion,
982 J., Willoughby, H., and Zhang, X.: Probing hurricanes with stable isotopes of
983 rain and water vapor, Mon. Weather Rev., 131, 1112-1127,

984 [https://doi.org/10.1175/1520-0493\(2003\)131<1112:Phwsio>2.0.Co;2](https://doi.org/10.1175/1520-0493(2003)131<1112:Phwsio>2.0.Co;2), 2003.

985 Goff, J.A., and Gratch, S.: Low-pressure properties of water from -160°F to 212 °F.
986 Transactions of the American Society of Heating and Ventilating Engineers, 52,
987 95-122, 1946.

988 Goswami, B.N., Venugopal, V., Sengupta, D., Madhusoodanan, M.S., and Xavier, P.K.:
989 Increasing Trend of Extreme Rain Events Over India in a Warming Environment,
990 Science, 314, 1442-1445, <https://doi.org/10.1126/science.1132027>, 2006.

991 Graf, P., Wernli, H., Pfahl, S., and Sodemann, H.: A new interpretative framework for
992 below-cloud effects on stable water isotopes in vapour and rain, Atmos. Chem.
993 Phys., 19, 747-765, <https://doi.org/10.5194/acp-19-747-2019>, 2019.

994 Guo, X., Tian, L., Wen, R., Yu, W., and Qu, D.: Controls of precipitation $\delta^{18}\text{O}$ on the
995 northwestern Tibetan Plateau: A case study at Ngari station, Atmos. Res., 189,
996 141-151, <https://doi.org/10.1016/j.atmosres.2017.02.004>, 2017.

997 Hersbach, H., Bell, B., Berrisford, P., Hirahara, S., Horányi, A., Muñoz Sabater, J.,
998 Nicolas, J., Peubey, C., Radu, R., Schepers, D., Simmons, A., Soci, C., Abdalla,
999 S., Abellan, X., Balsamo, G., Bechtold, P., Biavati, G., Bidlot, J., Bonavita, M.,
1000 and Thépaut, J.N.: The ERA5 global reanalysis, Q. J. Roy. Meteor. Soc.,
1001 <https://doi.org/10.1002/qj.3803>, 2020.

1002 Hsu, Y-K., Holsen, T.M., and Hopke, P.K.: Comparison of hybrid receptor models to
1003 locate PCB sources in Chicago, Atmos. Environ., 37, 545-562,
1004 [https://doi.org/10.1016/S1352-2310\(02\)00886-5](https://doi.org/10.1016/S1352-2310(02)00886-5), 2003.

1005 Jayasena, H.A.H., Chandrajith, R., and Dissanayake, C.B.: Spatial variation of isotope
1006 composition in precipitation in a tropical environment: a case study from the
1007 Deduru Oya river basin, Sri Lanka, Hydrol. Process., 22, 4565-4570,
1008 <https://doi.org/10.1002/hyp.7060>, 2008.

1009 Kaushal, N., Breitenbach, S.F.M., Lechleitner, F.A., Sinha, A., Tewari, V.C., Ahmad,
1010 S.M., Berkelhammer, M., Band, S., Yadava, M., Ramesh, R., and Henderson,
1011 G.M.: The Indian Summer Monsoon from a Speleothem $\delta^{18}\text{O}$ Perspective-A
1012 Review, Quaternary, 1, 29, <https://doi.org/10.3390/quat1030029>, 2018.

1013 Kostrova, S.S., Meyer, H., Fernandoy, F., Werner, M., and Tarasov, P.E.: Moisture
1014 origin and stable isotope characteristics of precipitation in southeast Siberia,
1015 *Hydrol. Process.*, 34, 51-67, <https://doi.org/10.1002/hyp.13571>, 2020.

1016 Kurita, N.: Origin of Arctic water vapor during the ice-growth season, *Geophys. Res.*
1017 *Lett.*, 38, <https://doi.org/10.1029/2010GL046064>, 2011.

1018 Kurita, N.: Water isotopic variability in response to mesoscale convective system over
1019 the tropical ocean, *J. Geophys. Res. Atmos.*, 118, 10,376-10,390,
1020 <https://doi.org/10.1002/jgrd.50754>, 2013.

1021 Landshuter, N., Aemisegger, F., Mölg, T.: Stable Water Isotope Signals and Their
1022 Relation to Stratiform and Convective Precipitation in the Tropical Andes, *J.*
1023 *Geophys. Res. Atmos.*, 129, e2023JD040630,
1024 <https://doi.org/10.1029/2023JD040630>, 2024.

1025 Lekshmy, P.R., Midhun, M., and Ramesh, R.: Influence of stratiform clouds on δD and
1026 $\delta^{18}\text{O}$ of monsoon water vapour and rain at two tropical coastal stations, *J.*
1027 *Hydrol.*, 563, 354-362, <https://doi.org/10.1016/j.jhydrol.2018.06.001>, 2018.

1028 Lekshmy, P.R., Midhun, M., and Ramesh, R.: Role of moisture transport from Western
1029 Pacific region on water vapor isotopes over the Bay of Bengal, *Atmos. Res.*,
1030 265, 105895, <https://doi.org/10.1016/j.atmosres.2021.105895>, 2022.

1031 Lekshmy, P.R., Midhun, M., Ramesh, R., and Jani, R.A.: ^{18}O depletion in monsoon rain
1032 relates to large scale organized convection rather than the amount of rainfall,
1033 *Sci. Rep.*, 4, 5661, <https://doi.org/10.1038/srep05661>, 2014.

1034 Liu, J., Ding, M., and Xiao, C.: Review on atmospheric water vapor isotopic
1035 observation and research: theory, method and modeling, *Prog. Geog.*, 34, 340-
1036 353, <https://doi.org/10.11820/dlkxjz.2015.03.009>, 2015.

1037 Liu, X., and Chen, B.: Climatic warming in the Tibetan Plateau during recent decades,
1038 *Int. J. Climatol.*, 20, 1729-1742, [https://doi.org/10.1002/1097-0088\(20001130\)20:14<1729::AID-JOC556>3.0.CO;2-Y](https://doi.org/10.1002/1097-0088(20001130)20:14<1729::AID-JOC556>3.0.CO;2-Y), 2000.

1040 Majoube, M.: Fractionnement en oxygène 18 entre la glace et la vapeur d'eau, *Journal*
1041 *De Chimie Physique*, 68, 625-636, 1971a.

1042 Majoube, M.: Fractionnement en oxygène 18 et en deutérium entre l'eau et sa vapeur,
1043 Journal de Chimie Physique et de Physico Chimie Biologique, 68, 1423-1436,
1044 <https://doi.org/10.1051/jcp/1971681423>, 1971b.

1045 Malmgren, B.A., Hulugalla, R., Hayashi, Y., and Mikami, T.: Precipitation trends in Sri
1046 Lanka since the 1870s and relationships to El Niño-southern oscillation, Int. J.
1047 Climatol., 23, 1235-1252, <https://doi.org/10.1002/joc.921>, 2003.

1048 Masunaga, H., and Kummerow, C.: Observations of tropical precipitating clouds
1049 ranging from shallow to deep convective systems, Geophys. Res. Lett., 33, 805,
1050 <https://doi.org/10.1029/2006GL026547>, 2006.

1051 Merlivat, L., and Jouzel, J.: Global climatic interpretation of the deuterium-oxygen 18
1052 relationship for precipitation, J. Geophys. Res. Oceans., 84, 5029-5033.
1053 <https://doi.org/10.1029/JC084iC08p05029>, 1979.

1054 Midhun, M., Lekshmy, P.R., and Ramesh, R.: Hydrogen and oxygen isotopic
1055 compositions of water vapor over the Bay of Bengal during monsoon, Geophys.
1056 Res. Lett., 40, 6324-6328, <https://doi.org/10.1002/2013GL058181>, 2013.

1057 Ohring, G., Gruber, A., and Ellingson, R.: Satellite Determinations of the Relationship
1058 between Total Longwave Radiation Flux and Infrared Window Radiance, J.
1059 Appl. Meteorol. Clim., 23, 416-425, [https://doi.org/10.1175/1520-0450\(1984\)023<0416:SDOTRB>2.0.CO;2](https://doi.org/10.1175/1520-0450(1984)023<0416:SDOTRB>2.0.CO;2), 1984.

1061 Pang, Z., Kong, Y., Froehlich, K., Huang, T., Yuan, L., Li, Z., and Wang, F.: Processes
1062 affecting isotopes in precipitation of an arid region, Tellus B, 63, 352-359,
1063 <https://doi.org/10.1111/j.1600-0889.2011.00532.x>, 2011.

1064 Permana, D.S., Thompson, L.G., and Setyadi, G.: Tropical West Pacific moisture
1065 dynamics and climate controls on rainfall isotopic ratios in southern Papua,
1066 Indonesia, J. Geophys. Res. Atmos., 121, 2222-2245,
1067 <https://doi.org/10.1002/2015JD023893>, 2016.

1068 Pfahl, S., and Wernli, H.: Air parcel trajectory analysis of stable isotopes in water vapor
1069 in the eastern Mediterranean, J. Geophys. Res., 113, D20104,
1070 <https://doi.org/10.1029/2008JD009839>, 2008.

1071 Pfahl, S., and Wernli, H.: Lagrangian simulations of stable isotopes in water vapor: An
1072 evaluation of nonequilibrium fractionation in the Craig-Gordon model, *J.
1073 Geophys. Res. Atmos.*, 114, 108, <https://doi.org/10.1029/2009JD012054>, 2009.

1074 Rahul, P., Ghosh, P., and Bhattacharya, S.K.: Rainouts over the Arabian Sea and
1075 Western Ghats during moisture advection and recycling explain the isotopic
1076 composition of Bangalore summer rains, *J. Geophys. Res. Atmos.*, 121, 6148-
1077 6163, <https://doi.org/10.1002/2015JD024579>, 2016a.

1078 Rahul, P., Ghosh, P., Bhattacharya, S.K., and Yoshimura, K.: Controlling factors of
1079 rainwater and water vapor isotopes at Bangalore, India: Constraints from
1080 observations in 2013 Indian monsoon, *J. Geophys. Res. Atmos.*, 121, 13,936-
1081 13,952, <https://doi.org/10.1002/2016JD025352>, 2016b.

1082 Ranjan, S., Al, R., Keesari, T., Singh, V., Kumar, P., and Manish Leuenberger, M.: Triple
1083 Water Vapour-Isotopologues Record from Chhota Shigri, Western Himalaya,
1084 India: A Unified Interpretation based on $\delta^{17}\text{O}$, $\delta^{18}\text{O}$, δD and Comparison to
1085 Meteorological Parameters, *Front. Earth Sci.*, 8, 599-632,
1086 <https://doi.org/10.3389/feart.2020.599632>, 2021.

1087 Ravisankar, L., Madhavan, M., and Ramesh, R.: Spatial variation of amount effect over
1088 peninsular India and Sri Lanka: Role of seasonality, *Geophys. Res. Lett.*, 42,
1089 5500-5507, <https://doi.org/10.1002/2015GL064517>, 2015.

1090 Risi, C., Bony, S., and Vimeux, F.: Influence of convective processes on the isotopic
1091 composition ($\delta^{18}\text{O}$ and δD) of precipitation and water vapor in the tropics: 2.
1092 Physical interpretation of the amount effect, *J. Geophys. Res. Atmos.*, 113, 306,
1093 <https://doi.org/10.1029/2008JD009943>, 2008.

1094 Risi, C., Galewsky, J., Reverdin, G., Brient, F.: Controls on the water vapor isotopic
1095 composition near the surface of tropical oceans and role of boundary layer
1096 mixing processes, *Atmos. Chem. Phys.*, 19, 19, <https://doi.org/10.5194/acp-19-12235-2019>, 2019.

1098 Risi, C., Muller, C., and Blossey, P.: What controls the water vapor isotopic composition
1099 near the surface of tropical oceans? Results from an analytical model

1100 constrained by large-eddy simulations. *J. Adv. Model. Earth Sy.*, 12,
1101 e2020MS002106, <https://doi.org/10.1029/2020MS002106>, 2020.

1102 Salamalikis, V., Argiriou, A.A., and Dotsika, E.: Stable isotopic composition of
1103 atmospheric water vapor in Patras, Greece: A concentration weighted trajectory
1104 approach, *Atmos. Res.*, 152, 93-104,
1105 <https://doi.org/10.1016/j.atmosres.2014.02.021>, 2015.

1106 Saranya, P., Krishan, G., Rao, M.S., Kumar, S., and Kumar, B.: Controls on water vapor
1107 isotopes over Roorkee, India: Impact of convective activities and depression
1108 systems, *J. Hydrol.*, 557, 679-687,
1109 <https://doi.org/10.1016/j.jhydrol.2017.12.061>, 2018.

1110 Schumacher, C.: Shallow tropical convection: How often does it rain? *Bull. Am.*
1111 *Meteorol. Soc.*, 87, 23-25, 2006.

1112 Singh, P., and Bengtsson, L.: Hydrological sensitivity of a large Himalayan basin to
1113 climate change, *Hydrol. Process.*, 18, 2363-2385,
1114 <https://doi.org/10.1002/hyp.1468>, 2004.

1115 Srivastava, R., Ramesh, R., Gandhi, N., Jani, R.A., and Singh, A.K.: Monsoon onset
1116 signal in the stable oxygen and hydrogen isotope ratios of monsoon vapor,
1117 *Atmos. Environ.*, 108, 117-124,
1118 <https://doi.org/10.1016/j.atmosenv.2015.02.062>, 2015.

1119 Steen-Larsen, H.C., Masson-Delmotte, V., Hirabayashi, M., Winkler, R., Satow, K.,
1120 Prié, F., Bayou, N., Brun, E., Cuffey, K., Dahl-Jensen, D., Dumont, M.,
1121 Guillevic, M., Kipfstuhl, J., Landais, A., Popp, T., Risi, C., Steffen, K., Stenni,
1122 B., and Sveinbjörnsdóttir, A.: What controls the isotopic composition of
1123 Greenland surface snow? *Clim. Past.*, 10, 379-392, <https://doi.org/10.5194/cpd-9-6035-2013>, 2013a.

1125 Steen-Larsen, H.C., Johnsen, S.J., Masson-Delmotte, V., Stenni, B., Risi, C., Sodemann,
1126 H., Balslev-Clausen, D., Blunier, T., Dahl-Jensen, D., Ellehøj, M.D., Falourd,
1127 S., Grindsted, A., Gkinis, V., Jouzel, J., Popp, T., Sheldon, S., Simonsen, S.B.,
1128 Sjolte, J., Steffensen, J.P., Sperlich, P., Sveinbjörnsdóttir, A.E., Vinther, B.M.,

1129 and White, J.W.C.: Continuous monitoring of summer surface water vapor
1130 isotopic composition above the Greenland Ice Sheet, *Atmos. Chem. Phys.*, 13,
1131 4815-4828, <https://doi.org/10.5194/acp-13-4815-2013>, 2013b.

1132 Steen-Larsen, H.C., Risi, C., Werner, M., Yoshimura, K., and Masson-Delmotte, V.:
1133 Evaluating the skills of isotope-enabled general circulation models against in
1134 situ atmospheric water vapor isotope observations, *J. Geophys. Res. Atmos.*,
1135 122, 246–263, <https://doi.org/10.1002/2016JD025443>, 2017.

1136 Steen-Larsen, H.C., Sveinbjörnsdóttir, A.E., Jonsson, T., Ritter, F., Bonne, J-L.,
1137 Masson-Delmotte, V., Sodemann, H., Blunier, T., Dahl-Jensen, D., and Vinther,
1138 B.M.: Moisture sources and synoptic to seasonal variability of North Atlantic
1139 water vapor isotopic composition, *J. Geophys. Res. Atmos.*, 120, 5757-5774,
1140 <https://doi.org/10.1002/2015JD023234>, 2015.

1141 Stewart, M.K.: Stable isotope fractionation due to evaporation and isotopic exchange
1142 of falling waterdrops: Applications to atmospheric processes and evaporation of
1143 lakes, *J. Geophys. Res.*, 80, 1133-1146,
1144 <https://doi.org/10.1029/JC080i009p01133>, 1975.

1145 Sturm, P., and Knohl, A.: Water vapor $\delta^2\text{H}$ and $\delta^{18}\text{O}$ measurements using off-axis
1146 integrated cavity output spectroscopy, *Atmos. Meas. Tech.*, 3, 67-77,
1147 <https://doi.org/10.5194/amt-3-67-2010>, 2010.

1148 Thompson, L.G., Davis, M.E., Mosley-Thompson, E., Beaudon, E., Porter, S.E.,
1149 Kutuzov, S., Lin, P.N., Mikhalenko, V.N., and Mountain, K.R.: Impacts of
1150 Recent Warming and the 2015/2016 El Niño on Tropical Peruvian Ice Fields, *J.*
1151 *Geophys. Res. Atmos.*, 122, 12,688-12,701,
1152 <https://doi.org/10.1002/2017JD026592>, 2017.

1153 Tremoy, G., Vimeux, F., Mayaki, S., Souley, I., Cattani, O., Risi, C., Favreau, G., and
1154 Oi, M.: A 1-year long $\delta^{18}\text{O}$ record of water vapor in Niamey (Niger) reveals
1155 insightful atmospheric processes at different timescales, *Geophys. Res. Lett.*,
1156 39(8), 805, <https://doi.org/10.1029/2012GL051298>, 2012.

1157 Thurnherr, I. and Aemisegger, F.: Disentangling the impact of air-sea interaction and

1158 boundary layer cloud formation on stable water isotope signals in the warm
1159 sector of a Southern Ocean cyclone, *Atmos. Chem. Phys.*, 22, 10353-10373,
1160 <https://doi.org/10.5194/acp-22-10353-2022>, 2022.

1161 Thurnherr, I., Hartmuth, K., Jansing, L., Gehring, J., Boettcher, M., Gorodetskaya, I.,
1162 Werner, M., Wernli, H., and Aemisegger, F.: The role of air-sea fluxes for the
1163 water vapour isotope signals in the cold and warm sectors of extratropical
1164 cyclones over the Southern Ocean, *Weather Clim. Dynam.*, 2, 331-357,
1165 <https://doi.org/10.5194/wcd-2-331-2021>, 2021.

1166 Thurnherr, I., Kozachek, A., Graf, P., Weng, Y., Bolshiyanov, D., Landwehr, S., Pfahl,
1167 S., Schmale, J., Sodemann, H., Steen-Larsen, H.C., Toffoli, A., Wernli, H., and
1168 Aemisegger, F.: Meridional and vertical variations of the water vapour isotopic
1169 composition in the marine boundary layer over the Atlantic and Southern Ocean,
1170 *Atmos. Chem. Phys.*, 20, 5811-5835, <https://doi.org/10.5194/acp-20-5811-2020>,
1171 2020.

1172 Uemura, R., Matsui, Y., Yoshimura, K., Motoyam, H., and Yoshida, N.: Evidence of
1173 deuterium excess in water vapor as an indicator of ocean surface conditions, *J.*
1174 *Geophys. Res. Atmos.*, 113, D19114, <https://doi.org/10.1029/2008JD010209>,
1175 2008.

1176 Villiger, L., and Aemisegger, F.: Water isotopic characterisation of the cloud-circulation
1177 coupling in the North Atlantic trades – Part 2: The imprint of the atmospheric
1178 circulation at different scales, *Atmos. Chem. Phys.*, 24, 957-976,
1179 <https://doi.org/10.5194/acp-24-957-2024>, 2024.

1180 Vimeux, F., Tremoy, G., Risi, C., and Gallaire, R.: A strong control of the South
1181 American SeeSaw on the intra-seasonal variability of the isotopic composition
1182 of precipitation in the Bolivian Andes, *Earth. Planet. Sci. Lett.*, 307, 47-58,
1183 <https://doi.org/10.1016/j.epsl.2011.04.031>, 2011.

1184 Wallace, J.M., and Hobbs, P.V.: 3-Atmospheric Thermodynamics, *Atmos. Sci.*, 63-111,
1185 <https://doi.org/10.1016/B978-0-12-732951-2.50008-9>, 2006.

1186 Wang, B.: The Asian monsoon. Springer praxis books, Springer/Praxis Publishing Co,

1187 Berlin, 787 pp., 651-683, 2006.

1188 Webster, P.J., Magana, V.O., Palmer, T.N., Shukla, J., Tomas, R.A., Yanai, M., and
1189 Yasunari, T.: Monsoons: Processes, predictability, and the prospects for
1190 prediction, *J. Geophys. Res. Oceans.*, 103, 14451-14510,
1191 <https://doi.org/10.1029/97JC02719>, 1998.

1192 Worden, J., Noone, D., Bowman, K., Beer, R., Eldering, A., Fisher, B., Gunson, M.,
1193 Goldman, A., Herman, R., Kulawik, S., Lampel, M., Osterman, G., Rinsland,
1194 C., Rodgers, C., Sander, S., Shephard, M., Webster, C., and Worden, H.:
1195 Importance of rain evaporation and continental convection in the tropical water
1196 cycle, *Nature*, 445, 528-532, <https://doi.org/10.1038/nature05508>, 2007. Xu, T.,
1197 Pang, H., Zhan, Z., Zhang, W., Guo, H., Wu, S., and Hou, S.: Water vapor
1198 isotopes indicating rapid shift among multiple moisture sources for the 2018-
1199 2019 winter extreme precipitation events in southeastern China, *Hydrol. Earth
1200 Syst. Sci.*, 26, 117-127, <https://doi.org/10.5194/hess-26-117-2022>, 2022.

1201 Yao, T., Thompson, L.G., Mosbrugger, V., Zhang, F., Ma, Y., Luo, T., Xu, B., Yang, X.,
1202 Joswiak, D.R., Wang, W., Joswiak, M.E., Devkota, L.P., Tayal, S., Jilani, R., and
1203 Chen, F.: Third Pole Environment (TPE), *Environ. Dev.*, 7, 52-64,
1204 <https://doi.org/10.1016/j.envdev.2012.04.002>, 2012.